# Fast and Efficient Optical Phase Conjugation Using a Degenerate Raman System in Rubidium

by

Darren S. Hsiung

Scientiae Baccalaureus, M.I.T. (1997)

Submitted to the Department of Electrical Engineering and Computer Science in partial fulfillment of the requirements for the degree of

Master of Engineering

at the

MASSACHUSETTS INSTITUTE OF TECHNOLOGY

September 1997



Author .....
Department of Electrical Engineering and Computer Science
August 8, 1997

Certified by .....
Shaoul Ezekiel
Professor of Electrical Engineering & Aeronautics and Astronautics
Thesis Supervisor

Certified by .....
Selim M. Shahriar
Research Scientist, Research Laboratory of Electronics
Thesis Supervisor

Accepted by .....
Arthur C. Smith
Chairman, Department Committee on Graduate Theses

# Fast and Efficient Optical Phase Conjugation Using a Degenerate Raman System in Rubidium

by

Darren Hsiung

Submitted to the Department of Electrical Engineering and Computer Science on August 8, 1997, in partial fulfillment of the requirements for the degree of Master of Engineering

## Abstract

Fast, efficient, and low power optical phase conjugation (OPC) is of interest for many applications such as aberration correction in real-time holography and optical resonators. Previous work in degenerate OPC generation using two-level Na atoms required high power levels (>1 W), yielded low gain (~2), and required bulky dye lasers to attain the transition wavelength. This thesis demonstrates OPC via degenerate four-wave mixing in rubidium using Zeeman sublevels in a single hyperfine transition to form a $\Lambda$ system. This system is pumped with cross-circularly polarized light. The resulting optical phase conjugator required low power (<100 mW), was fast (response time of 160 ns) and efficient (gain as high as 40), and used a transition wavelength attainable with semiconductor lasers (794.98 nm), allowing the system to be very practical. The maximum conjugate gain was measured at a frequency blue-shifted from the $5^2S_{1/2}$, $f$=2 $\rightarrow$ $5^2P_{1/2}$, $f$=1 transition, indicating the participation of nonzero velocity atoms in the process. To demonstrate the application of this high gain degenerate system in creating an inherently frequency stable laser, a preliminary experiment was carried out and lasing was observed. The details of such a laser should be investigated in the future.

Thesis Supervisor: Shaoul Ezekiel
Title: Professor of Electrical Engineering & Aeronautics and Astronautics

Thesis Supervisor: Dr. Selim M. Shahriar
Title: Research Scientist, Research Laboratory of Electronics

# Acknowledgments

I wish to thank a number of people without whom, this thesis may not have been possible. First I wish to thank Professor Shaoul Ezekiel for the opportunity to work under him on this research project. I also thank Dr. Selim Shariar for all his guidance and motivational speeches, encouraging me to push myself to give my best for my work.

I would also like to thank my colleagues in the lab. Dr. Timothy Grove taught me practically everything I know about the lab equipment and machine shop tools. His wealth of anecdotes helped ensure that lab would never get too dull. Dr. Xiao-Wei Xia has been an invaluable and patient partner in setting up and running the experiments. I have also enjoyed our numerous conversations about philosophy and religion. I also thank Phil Hemmer and V. S. "Sudi" Sudarshanam for their support. John Kierstead offered much technical support and safety advice, without which I might be short my retina and one or two appendages. Furthermore, I wish to thank Emmanuel Rousseau, Yuli Friedman, and Niell Elvin for assuring me that I was not the only clueless person in the group's seminars.

A number of people outside the research group have also been greatly supportive. I wish to thank all my brothers and sisters in the Lord, including David Sun, Loren Shih, David Shue, Eric Ding, Bryan Che, Shiu-Chung Au, Rita Leung and Hubert Siu for prayer and accountability. I thank Lucia Wu for taking enough interest in my work to help me proofread this thesis. She was patient enough to listen as I blabbered on about my work, when most would have asked me to put a clam on it. I thank Jasen Li for showing me what being a brother is truly about. His example in living has led me to want to love God more. Sharon Ng has been an encourager to me, continually upholding me in prayer despite the distance. And I thank Mom and Dad for loving me even as I drain their life savings, all in the name of higher education.

Finally I give all glory and praise to Jesus Christ who keeps me near in His grace, under the shadow of the cross.

*Near the cross I'll watch and wait,*
*Hoping, trusting ever,*
*'til I reach the golden strand*
*Just beyond the river.*
*-Fanny J. Crosby*

# Table of Contents

# List of Figures

## Chapter 2



## Chapter 3



## Chapter 4

## Chapter 5

# List of Tables

## Chapter 1



## Chapter 2

# Chapter 1

# Introduction

## 1.1 Motivation and Objective

Phase conjugate optics applied to optical resonators has interesting consequences in laser systems. A phase conjugate mirror (PCM) opposite the output coupler can be used to correct distortion within the resonator cavity. This greatly improves the laser beam's spatial quality and optimizes output from the gain medium [1]. The phase conjugate optical resonator is also stable regardless of cavity length and mirror curvature, thus reducing the laser's sensitivity to misalignment.

In order to implement a reasonable phase conjugate optical resonator, the properties of the PCM medium are important to investigate. A fast response time and high gain in the reflectivity are issues of concern. For practical purposes, a system accessible to the frequency and power range of diode lasers, which are less expensive and easier to maintain than dye lasers, is desirable.

This work implements an optical resonator using a degenerate Raman $\Lambda$ system in rubidium as the PCM. Although the non-degenerate case yields a higher gain [2], the resultant frequency shift in the conjugate beam makes a lasing system much more difficult to realize. Since all the transition frequencies are theoretically the same in the degenerate case, it is easy to make the conjugate beam look identical to the incident probe beam when fed back into the system.

## 1.2 Background

Optical phase conjugation (OPC) can be achieved through a number of techniques and nonlinear optical media. OPC has been observed in degenerate four-wave mixing, three-wave mixing, scattering from saturated sources, photon echoes, stimulated Brillouin

scattering and stimulated Raman scattering. Table 1.1 compares properties of a number of materials used for OPC. The first four materials have major drawbacks in slow response time $\tau_r$, high power requirement, or low efficiency.

| Material | $\tau_r$ | Intensity$_{th}$(W/cm$^2$) | Reflectivity |
|---|---|---|---|
| Brillouin Scattering | 1-10 ns | $10^6$ - $10^7$ | 1 |
| Quantum Well | 1 ps-1 μs | 1 | 0.03 |
| Two-level Na | 10-100 ns | 100 | 2-3 |
| Photorefractive ($BaTiO_3$) | 10 ms | < 1 | 10 |
| Double Λ Na | < 1 μs | 1 | 50 |
| Double Λ Rb | 60 ns | 1 | 3 |

**Table 1.1: Properties of various OPC media**

The method of obtaining OPC relevant to this work is four-wave mixing. Resonant atomic systems are a good choice for the nonlinear medium because they are fast [3]. Previously, sodium has been used successfully in phase conjugation experiments [3,4,5]. However, atomic systems are generally less efficient than photorefractive crystals which have also been used to generate OPC. Experiments have used coherent population trapping in the Raman system to sacrifice a little speed for higher efficiency [6].

Recent work used $^{87}$Rb, which has a hyperfine manifold identical to that of sodium. This is a simpler and better approach because coherent population trapping occurs between Zeeman sublevels as opposed to hyperfine sublevels. The transition wavelength between the levels of interest in rubidium ($5^2S_{1/2}$, F=2; $5^2P_{1/2}$, F=1) is around 794.98 nm, which is easily attainable with semiconductor lasers. The power of the reflected conjugate beam of this PCM is found to be almost 300 times that of the incident probe beam at low beam intensities [2]. In all of these cases, the levels in the Raman systems are nondegenerate and thus require detuning of the laser beams interacting in the system.

## 1.3 Scope

This thesis begins by investigating the properties of the degenerate Raman system in rubidium as a PCM. These properties include the dependence of the reflectivity on the probe beam power as well as the conjugate beam's dependence on the driving laser frequency, a magnetic field applied on the atomic system, and the pump beam polarization. These properties are then investigated for an optical resonator set up in a ring configuration. The grand finale is the valiant attempt to set up an effective linear standing wave resonator cavity.

Chapter 2 introduces the concept of OPC and PCMs in resonator cavities for those who may have been completely lost in the introduction. Chapter 3 provides a brief treatment on the physics of the Raman interaction in the $\Lambda$ system and assumes some knowledge in quantum mechanics. The advanced reader may glance through these chapters to refresh his memory (or laugh hysterically), or may choose to skip ahead to chapter 4, which describes the experimental set-up. The thoroughly impatient reader may go directly to chapter 5 to see the experimental results. The desperate fellow graduate student may just look at the conclusions in chapter 6 to gain ideas for future research projects.

# Chapter 2

# Introduction to the Phase Conjugate Optical Cavity

## 2.1 Optical Phase Conjugation

### 2.1.1 OPC for the Masses

Optical phase conjugation is a nonlinear optical effect that has curious consequences. For the sake of this treatment, we will only deal with OPC via four-wave mixing, which is a third order nonlinear effect. As the name of this process implies, four waves interact in a medium. These four light beams are the following:

- the *forward pump*, denoted as "F";
- the *backward pump*, denoted as "B";
- the *probe beam*, denoted as "P";
- the *conjugate beam*, denoted as "C", a beam resulting from the interactions of the other three.

The two pump beams are strong compared to the probe. For the sake of simplicity, we idealize the model so that the pump beams exactly counterpropagate, and so that all the beams have the same frequency. The geometry of these beams is shown in figure 2.1.

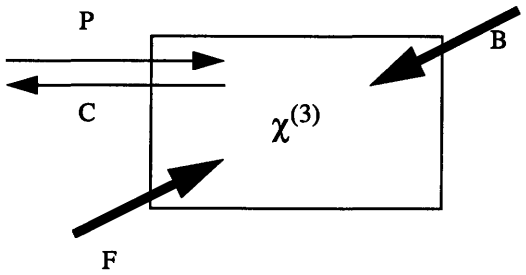


**Figure 2.1:** Four-wave mixing geometry in the phase conjugate mirror.

If we scratch away at the surface of the phase matching conditions for this system, we find two fundamental laws in physics: conservation of energy and conservation of momentum:

$$\omega_F + \omega_P + \omega_B + \omega_C = 0 \tag{2.1}$$

$$\vec{k}_F + \vec{k}_P + \vec{k}_B + \vec{k}_C = 0 \tag{2.2}$$

When all the necessary conditions are met, we see interesting consequences. The overall phase factor and the propagation direction of the conjugate beam are exactly the reverse of the probe beam; in other words, the conjugate beam's wavefront traces the time-reversed path of the probe beam. Because of this, OPC is sometimes referred to as wavefront reversal [7].

In order to get a firmer grasp on this concept, refer to figure 2.2. For a regular mirror, as shown in figure 2.2(a), the wavefront follows rather intuitive behavior: whatever reaches the mirror first is reflected first, and the angle of incidence is equal to the angle of

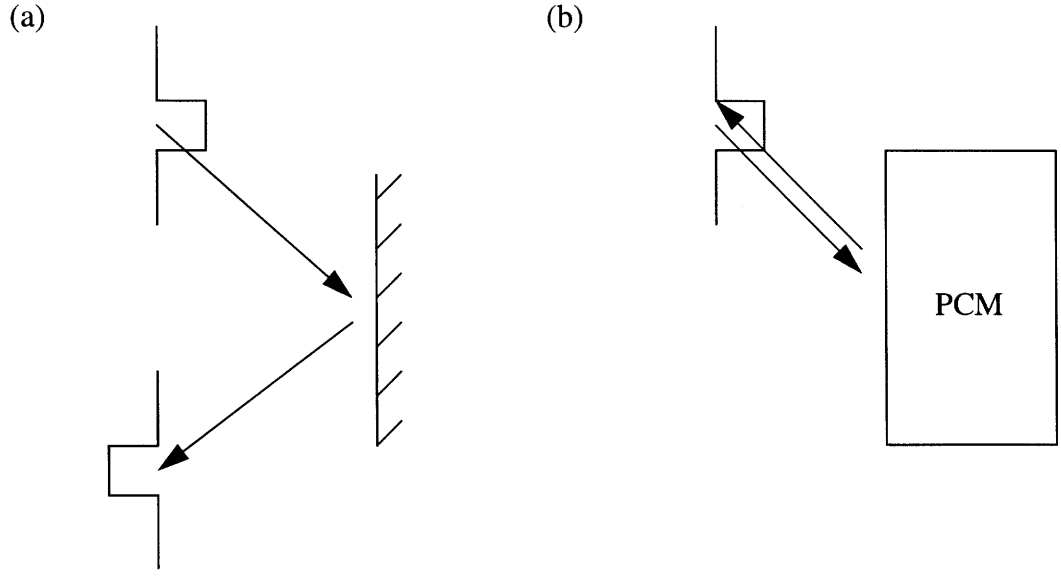


**Figure 2.2:** Reflection from (a) a normal mirror, (b) a phase conjugate mirror.

reflection. However, the behavior of the wavefront reflecting from a phase conjugate mirror is like that of running a movie projector in reverse. A man may see his face with a regular mirror, but he would only see his own pupils with a phase conjugate mirror.

### 2.1.2 The Generating Process

As with all nonlinear optical processes, the beams are intense enough to alter the characteristics of the medium. Thus one can model the interaction as a diffraction grating formed in the medium by the probe beam and one of the pump beams, with the conjugate beam resulting as the other pump beam scatters off the grating. Figure 2.3 illustrates this.

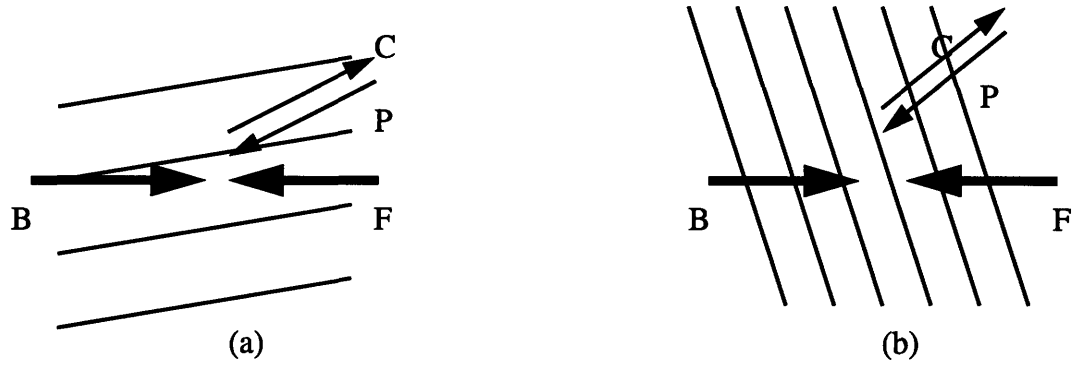


**Figure 2.3:** Conjugate generation by scattering from a grating. (a) The backward beam scatters off a grating formed by the interference of the forward and the probe beams, (b) The forward beam backscatters off a grating formed by the backward and probe beams.

The conjugate beam's energy comes from the pump beams and not the probe beams. Along with the generation of the conjugate beam, the scattering also results in the amplification of the probe beam. It is important to note that the grating configuration in figure 2.3(b) has a small spatial period and therefore is easily destroyed by small perturbations in the medium. Thus the configuration in figure 2.3(a) is the dominant model.

### 2.1.3 Mathematical View

In the most basic form, we can model an ideal PCM with monochromatic input. As before, assume that the pump beams are exactly counterpropagating and that the beams are plane

waves with the same frequency. Let $E_P$ be the field of the probe beam, and $\psi$ be the field amplitude. Thus we can write the input as

$$\vec{E_P}(\vec{r}, t) = Re\{\vec{\varepsilon}\psi(\vec{r})e^{i(\vec{k}\cdot\vec{r}-\omega t)}\} \tag{2.3}$$

which results in the field of the conjugate beam,

$$\vec{E_C}(\vec{r}, t) = Re\{\vec{\varepsilon}^*\rho\psi^*(\vec{r})e^{-i(\vec{k}\cdot\vec{r}+\omega t)}\} \tag{2.4}$$

where $\rho$ is the reflection coefficient of the PCM. Other than this extra factor, we note two main differences between the probe and conjugate beams. First, the field amplitude is replaced by its complex conjugate, resulting in wavefront reversal as indicated in figure 2.2. Second, the propagation vector reverses signs, indicating that the conjugate beam exactly falls on the probe beam path [8].

In calculating the amplification of the probe and conjugate beams in the four-wave mixing problem, it is useful to specify three more assumptions in the analysis: the material is isotropic, absorption is negligible, and the probe beam (and thus also the conjugate beam) propagates along the z-axis. From the basic wave equations and the nonlinear polarization, we can derive expressions for the field amplitudes for the transmitted probe and the reflected conjugate [9]:

$$\frac{d\psi_P}{dz} = -i\frac{2\pi\omega}{cn}\chi^{(3)}\psi_F\psi_B\psi_C^* \tag{2.5}$$

$$\frac{d\psi_C}{dz} = i\frac{2\pi\omega}{cn}\chi^{(3)}\psi_F\psi_B\psi_P^* \tag{2.6}$$

where $\omega$ is the frequency of the beams, $\chi^{(3)}$ is the nonlinear susceptibility, $n$ is the index of refraction of the medium, and $c$ is the speed of light in vacuum. We can simplify the appearance of the equations by defining

$$\kappa^* \equiv \frac{2\pi\omega}{cn}\chi^{(3)}\psi_F\psi_B. \tag{2.7}$$

Substituting (2.7) into equations (2.5) and (2.6) we can write

$$\frac{d}{dz}\psi_P^* = i\kappa\psi_C \tag{2.8}$$

$$\frac{d\psi_C}{dz} = i\kappa^*\psi_P^*. \tag{2.9}$$

This simple system of differential equations is easily solved when given the boundary conditions. For a length $L$ over which the beams interact, $\psi_P(z=0) = \psi$ as given in equation (2.3) is known, and $\psi_C(z=L) = 0$. Solving these equations, the amplitudes are

$$\psi_P(z) = -i\frac{|\kappa|\sin|\kappa|z}{\kappa\cos|\kappa|L}\psi_C^*(L) + \frac{\cos|\kappa|(z-L)}{\cos|\kappa|L}\psi_P^*(0) \tag{2.10}$$

$$\psi_C(z) = \frac{\cos|\kappa|z}{\cos|\kappa|L}\psi_C(L) + i\frac{\kappa^*\sin|\kappa|(z-L)}{|\kappa|\cos|\kappa|L}\psi_P^*(0) \tag{2.11}$$

therefore the amplitudes of the transmitted probe and the reflected conjugate are respectively

$$\psi_P(L) = \frac{\psi_P(0)}{\cos|\kappa|L} \tag{2.12}$$

$$\psi_C(0) = -i\left(\frac{\kappa^*}{|\kappa|}\tan|\kappa|L\right)\psi_P^*(0) \tag{2.13}$$

and the intensities of these beams are

$$I_P(L) = \frac{I_P(0)}{\cos^2|\kappa|L} \tag{2.14}$$

$$I_C(0) = I_P(0)\cdot\tan^2|\kappa|L. \tag{2.15}$$

From these results, we see that the probe beam is always amplified and that the reflectivity of the PCM is greater than one when

$$\frac{\pi}{4} \le |\kappa|L \le \frac{3\pi}{4}. \tag{2.16}$$

### 2.1.4 OPC in the Real World

Optical phase conjugation has many interesting applications. One of its better known uses is for the correction of aberrations in an optical system, such as turbulence in the earth's atmosphere. Figure 2.4 demonstrates how this is done. The wavefront is distorted after passing through the aberrating medium. However, the reflection from the phase conjugate mirror follows the time-reversed path back through the aberrating medium to reconstruct the original wavefront. The process can be fast enough to work even if the medium changes with time (e.g. turbulent atmosphere). This property has extended itself to applications such as automatic tracking, interferometers and fiber-optic gyroscopes.

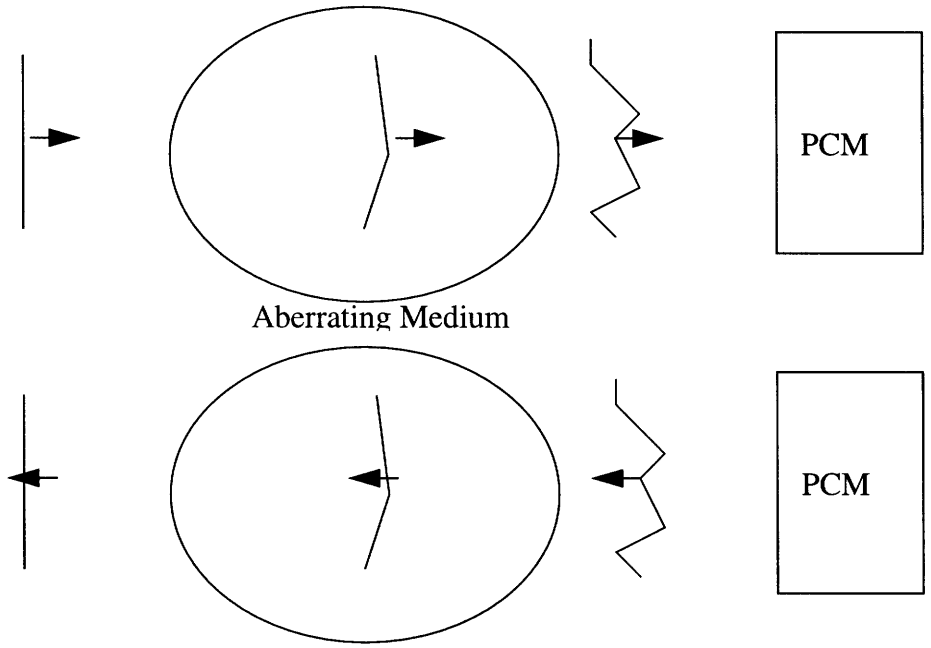


**Figure 2.4:** Aberration correction with a phase conjugate mirror.

Another useful aspect of OPC is that it is analogous to real-time holography. A holograph is essentially a diffraction grating etched into a material by the interference of a strong beam and a beam containing the image (analogous to the forward pump and the probe beams). The hologram is read by scattering another strong beam off the grating (analogous to the backward beam). The advantage of using OPC instead of conventional

holography is that OPC eliminates the need to create a hologram. Thus technologies such as real-time optical data storage and retrieval are possible.

The four-wave mixing process which generates OPC can also generate squeezed states of light. Essentially, squeezing involves an exchange, reducing the noise in part of the light wave while simultaneously increasing the noise in another part. Thus OPC can be used to make high precision measurements, as it surpasses the fundamental quantum uncertainty due to random fluctuations in the vacuum field.

The application explored in this thesis is OPC applied to the laser resonator, which we will now discuss.

## 2.2 The Optical Resonator

### 2.2.1 Primer

The primary use of an optical resonator is to build up large field intensities with smaller inputs [10]. This is accomplished by using two or more mirrors to form a cavity that stores the energy through multiple reflections. The optical beam thus falls into a mode of the resonator. For a laser cavity, these multiple reflections provide feedback through a gain medium that amplifies the beam (see figure 2.5). To utilize the laser beam outside the cavity, a beamsplitter can replace one of the mirrors.

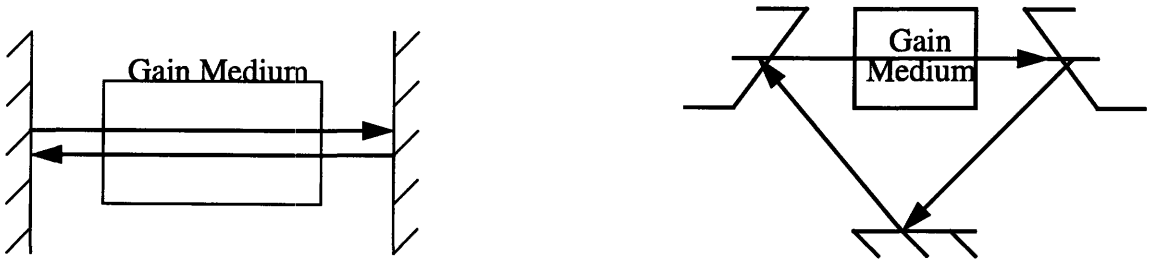


**Figure 2.5:** (a) standing wave cavity (b) ring laser cavity.

In a real system, a number of issues reduce the quality factor $Q$ of the cavity. The quality factor is a typical measure of a resonator and is defined as

$$Q = \omega \times (\textit{field energy stored})/(\textit{power dissipated}) \tag{2.17}$$

As the beam propagates in the cavity, it diffuses transversely. Thus there is diffraction loss as parts of the beam spill over the sides of the mirrors (unless you have infinitely large mirrors, which do not exist in this world). Curved mirrors can help refocus the beam to minimize diffraction loss. For low-order transverse modes in symmetric resonators, the diffraction loss is small when the Fresnel number $N > 1$, where $N$ is defined by the relation

$$N = \frac{a^2}{\lambda l} \tag{2.18}$$

where $a$ is the mirror radius (size, not curvature), $l$ is the separation of the mirrors, and $\lambda$ is the wavelength of the light.

With a high Fresnel number, the realm of geometric optics is a reasonable model for the optical system. A geometric description of the optical resonator stability condition is

$$0 \le \left(1 - \frac{l}{R_1}\right)\left(1 - \frac{l}{R_2}\right) \le 1 \tag{2.19}$$

where $R_1$ and $R_2$ are the radii of curvature of the mirrors. The optical beam inside a stable resonator cavity stays close to the optic axis after travelling long path lengths. Under stable conditions, the beam modes are Hermite-Gaussian.

Higher order transverse modes complicate issues because they experience greater diffraction loss and because cavity resonance conditions are affected by spatial modes. There are two primary methods of dealing with the divergence of the radiation due to these modes. One involves using a diaphragm, which lets through the $TEM_{00}$ (transverse electro-magnetic) mode and causes high losses in other modes. The other uses unstable resonators, which cause high losses in all modes, yet greater loss for the higher order

modes. The latter method yields a lousy quality factor and is only useful for high power applications (or there would not be enough power to cause lasing in the first place). The former method encounters problems if the resonator elements cause aberrations in the optical beam, thus requiring a smaller diaphragm to deal with the problem. Again, this lowers the quality factor of the resonator.

The next section will show how using a PCM in the resonator can address these issues.

### 2.2.2 Analysis of the PC Optical Resonator

This section contains a simple conceptual treatment for the phase conjugate optical resonator based on an analysis found in Yariv's book [9]. For a more rigorous mathematical treatment using the ABCD Gaussian mode formalism, please look up the references [9,11].

For the first analysis, we follow the phase of an arbitrary Gaussian beam propagating in a resonant standing wave cavity with a PCM. Figure 2.6(a) demonstrates this. The phase will change each time it reflects off the ordinary mirror, each time it travels across the cavity, and each time it reflects off the PCM. We label these changes in phase $\phi_R$ (dependent on the radius of curvature of the mirror), $\phi_l$ (dependent on the length of the cavity and the transverse modes of the beam), and $\alpha$ (dependent on the properties of the PCM) respectively. We choose a point next to the ordinary mirror as the starting point and arbitrarily call the phase $\phi$.

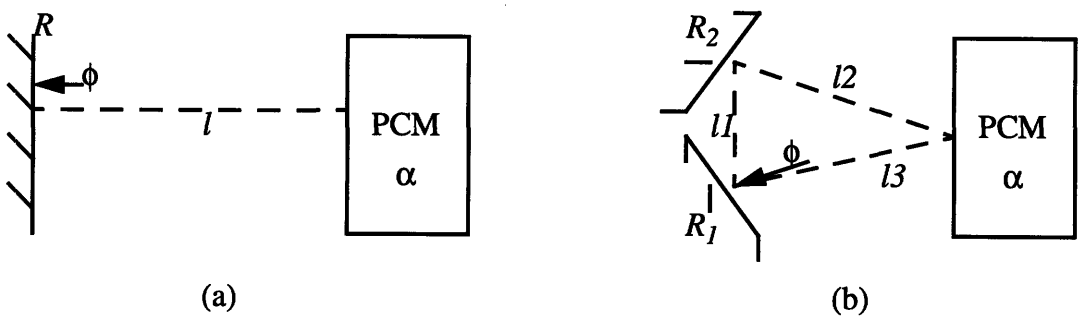


**Figure 2.6:** Phase conjugate optical resonator (a) standing wave (b) ring.

It is easiest to follow the phase at the various stages by organizing a table:

| Stage | Event | Phase |
|---|---|---|
| 1 | Start | $\phi$ |
| 2 | Reflection off Mirror $R$ ($+\phi_R$) | $\phi + \phi_R$ |
| 3 | Travel across cavity ($+\phi_l$) | $\phi + \phi_R + \phi_l$ |
| 4 | PCM reflection ($\times(-1)$; $+\alpha$) | $\alpha - \phi - \phi_R - \phi_l$ |
| 5 | Travel across cavity ($+\phi_l$) | $\alpha - \phi - \phi_R$ |
| 6 | Reflection off Mirror $R$ ($+\phi_R$) | $\alpha - \phi$ |
| 7 | Travel across cavity ($+\phi_l$) | $\alpha - \phi + \phi_l$ |
| 8 | PCM reflection ($\times(-1)$; $+\alpha$) | $\phi - \phi_l$ |
| 9 | Travel across cavity ($+\phi_l$) | $\phi$ |

**Table 2.1: Phase progression in the standing wave PCM resonator**

Remember that the PCM reflection is a wavefront reversal, which switches the sign of the phase of the incident beam. We see that by the ninth stage, after two round trips, the beam is not only back to where it began, but it also has the same phase from the beginning. Thus the phase conjugate resonator automatically satisfies a self-consistent condition and has a resonant frequency equal to that of the pump beams (of course we still assume that the PCM system is degenerate). This indicates that this system satisfies the resonance condition, regardless of the length of the cavity or the transverse mode of the beam.

Also, by following the path of the beam, and by taking the reversal due to the PCM into account, it is not hard to see that the shape and size of the wavefront after two round trips are also identical to those at the beginning. Thus we see that this system is inherently stable, regardless of the curvature of the mirror or the length of the cavity. It is important to note that for the nondegenerate case of the PCM (pump beams of different frequency), stability is not taken for granted [11].

Two headaches have been addressed so far by the PCM. Finally, we address the problem of aberrations in the resonator. But this is familiar (see section 2.1.4). The PCM corrects the distortion caused by the aberrating elements in the optical system. In the case mentioned in the previous section of removing higher order transverse modes using a diaphragm, there is no longer a need to reduce the size of the diaphragm. The resonator's $Q$ factor is preserved. For our model, we can think in terms of

$$\text{PCM} + \text{optical inhomogeneities} = \text{PCM}. \tag{2.20}$$

A similar analysis done on the ring resonator (figure 2.6(b)) will yield similar results.

| Stage | Event | Phase |
|---|---|---|
| 1 | Start | $\phi$ |
| 2 | Reflection off Mirror *R1* ($+\phi_{R1}$) | $\phi + \phi_{R1}$ |
| 3 | Travel across cavity *l1* ($+\phi_{l1}$) | $\phi + \phi_{R1} + \phi_{l1}$ |
| 4 | Reflection off Mirror *R2* ($+\phi_{R2}$) | $\phi + \phi_{R1} + \phi_{R2} + \phi_{l1}$ |
| 5 | Travel across cavity *l2* ($+\phi_{l2}$) | $\phi + \phi_{R1} + \phi_{R2} + \phi_{l1} + \phi_{l2}$ |
| 6 | PCM reflection ($\times(-1)$; $+\alpha$) | $\alpha - \phi - \phi_{R1} - \phi_{R2} - \phi_{l1} - \phi_{l2}$ |
| 7 | Travel across cavity *l3* ($+\phi_{l3}$) | $\alpha - \phi - \phi_{R1} - \phi_{R2} - \phi_{l1} - \phi_{l2} + \phi_{l3}$ |
| 8 | Reflection off Mirror *R1* ($+\phi_{R1}$) | $\alpha - \phi - \phi_{R2} - \phi_{l1} - \phi_{l2} + \phi_{l3}$ |
| 9 | Travel across cavity *l1* ($+\phi_{l1}$) | $\alpha - \phi - \phi_{R2} - \phi_{l2} + \phi_{l3}$ |
| 10 | Reflection off Mirror *R2* ($+\phi_{R2}$) | $\alpha - \phi - \phi_{l2} + \phi_{l3}$ |
| 11 | Travel across cavity *l2* ($+\phi_{l2}$) | $\alpha - \phi + \phi_{l3}$ |
| 12 | PCM reflection ($\times(-1)$; $+\alpha$) | $\phi - \phi_{l3}$ |
| 13 | Travel across cavity *l3* ($+\phi_{l3}$) | $\phi$ |

**Table 2.2: Phase progression in the ring PCM resonator**

This configuration, where the conjugate reflection does not fall back on the path of the incident beam, is easy to realize simply by putting an angle between the two pump beams.

This analysis deals with a system with two ordinary mirrors. We can extend this to a ring resonator with $n$ mirrors and find that the properties are unchanged. Again, after two round trips, the phase, beam shape and beam size are identical to the original. Thus this resonator is still stable and still meets the resonance condition. However, since the conjugate reflection does not retrace the path of the incident beam, this laser lacks the ability to correct aberrations due to optical inhomogeneities in the system.

# Chapter 3

# The Resonant Atomic System

## 3.1 Angular Momentum and Atomic Structure of Rubidium

### 3.1.1 Meet the Atom

The OPC medium with which this thesis is concerned is a vapor of neutral rubidium atoms. Conditions are such that each atom can be treated as a nearly isolated system. Rubidium is the $37^{th}$ element on the periodic table, in the family of alkali metals. In the ground state, it has 36 electrons in closed shells and one valence electron in the 5S orbital. Due to the single valence electron, rubidium falls into the category of Rydberg atoms, and can be considered "hydrogen-like" in the analysis. The two stable isotopes of Rubidium are $^{85}$Rb and $^{87}$Rb.

### 3.1.2 The Energy Eigenstates

Quantum mechanics gives us the eigenvalue equations for the square of the total angular momentum $\boldsymbol{F}^2$ and for the component of the angular momentum $F_z$ in some direction $z$

$$\hat{F} \cdot \hat{F}|f, m_f\rangle = \hat{F}^2|f, m_f\rangle = f(f+1)\bar{h}^2|f, m_f\rangle \tag{3.1}$$

$$\hat{F}_z|f, m_f\rangle = m_f\bar{h}|f, m_f\rangle \tag{3.2}$$

where $f$ is an integer or a half-integer and $m_f$ ranges from $-f, -f+1, \ldots, f-1, f$, for a total of $2f+1$ possible values; $\bar{h}$ is $h/2\pi$, where h is Planck's constant, $6.626 \times 10^{-27}$ erg•s or in units more appropriate to atomic measures, $4.136 \times 10^{-15}$ eV•s. In the absence of external fields, eigenstates with the same value of $f$ are degenerate regardless of their magnetic quantum number $m_f$. Degenerate simply means that they have the same energy. But when an external magnetic field is applied, the energies of these states shift, breaking the degeneracy. This is because charged particles in the atom have angular momentum, resulting in a magnetic moment. The magnetic moment of the atom is given by

$$\hat{\mu} = g_f \frac{e}{2mc} \hat{F} \tag{3.3}$$

where $e$ is the magnitude of the electron charge, $m$ is the electron mass, and $g_f$ is the Landé g-factor. The perturbation in the Hamiltonian of the system due to an applied external field is

$$\hat{H}_B = -\hat{\mu} \cdot \hat{B}. \tag{3.4}$$

For an external magnetic field that is weak in comparison to the internal fields of the atom, the atom's properties are not changed significantly. Thus for a constant magnetic field applied in the $z$ direction, the energy shifts of the eigenstates depend linearly on the magnetic field strength.

$$\Delta E = g_g \mu_B m_f B \tag{3.5}$$

Here, $\mu_B$ is a constant known as the Bohr magneton and is equal to $eh/4\pi mc$. The Landé g-factor is a proportionality constant dependent on the quantum numbers of the particular state. This level splitting due to an external magnetic field is known as Zeeman splitting.

The structure of the levels of interest are shown in figures 3.1 and 3.2. Note that the figure is not drawn to scale. It may be helpful to begin by defining the specific angular momenta. Angular moment is quantized in units of $\hbar$. The operator is written upper-case, the quantum number value is written lower-case.

- ☞ $\boldsymbol{L}$ is the orbital angular momentum
- ☞ $\boldsymbol{S}$ is the intrinsic angular momentum of the electron, otherwise known as spin
- ☞ $\boldsymbol{J}$ is the total of $\boldsymbol{L}$ and $\boldsymbol{S}$
- ☞ $\boldsymbol{I}$ is the intrinsic angular momentum of the nucleus, or the nuclear spin
- ☞ $\boldsymbol{F}$ is the total angular momentum

The qualitative explanations of the low-energy atomic phenomena relevant to this thesis are as follows, in order of decreasing energy.

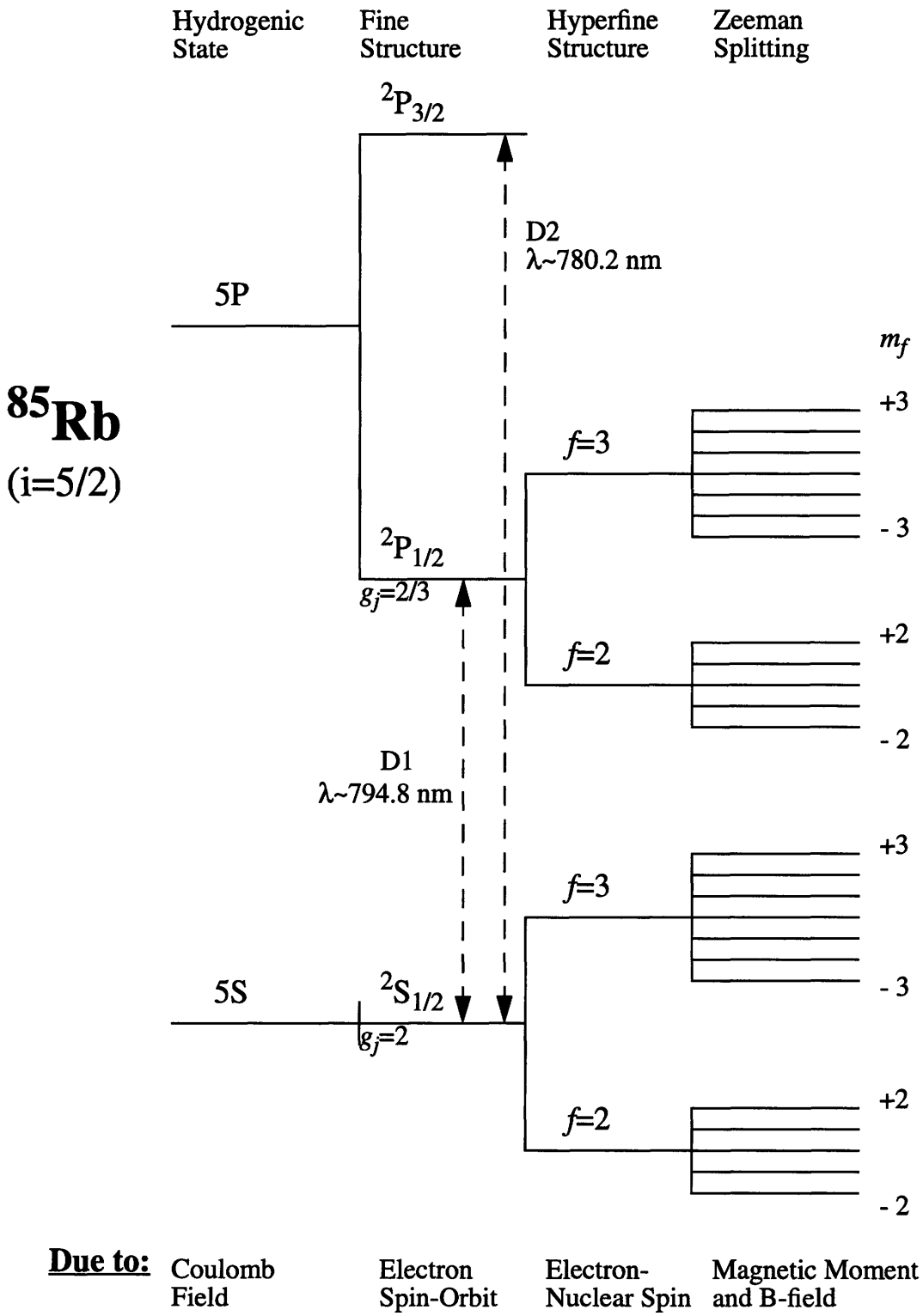


**Figure 3.1:** Schematic energy level diagram (not to scale) of $^{85}$Rb.

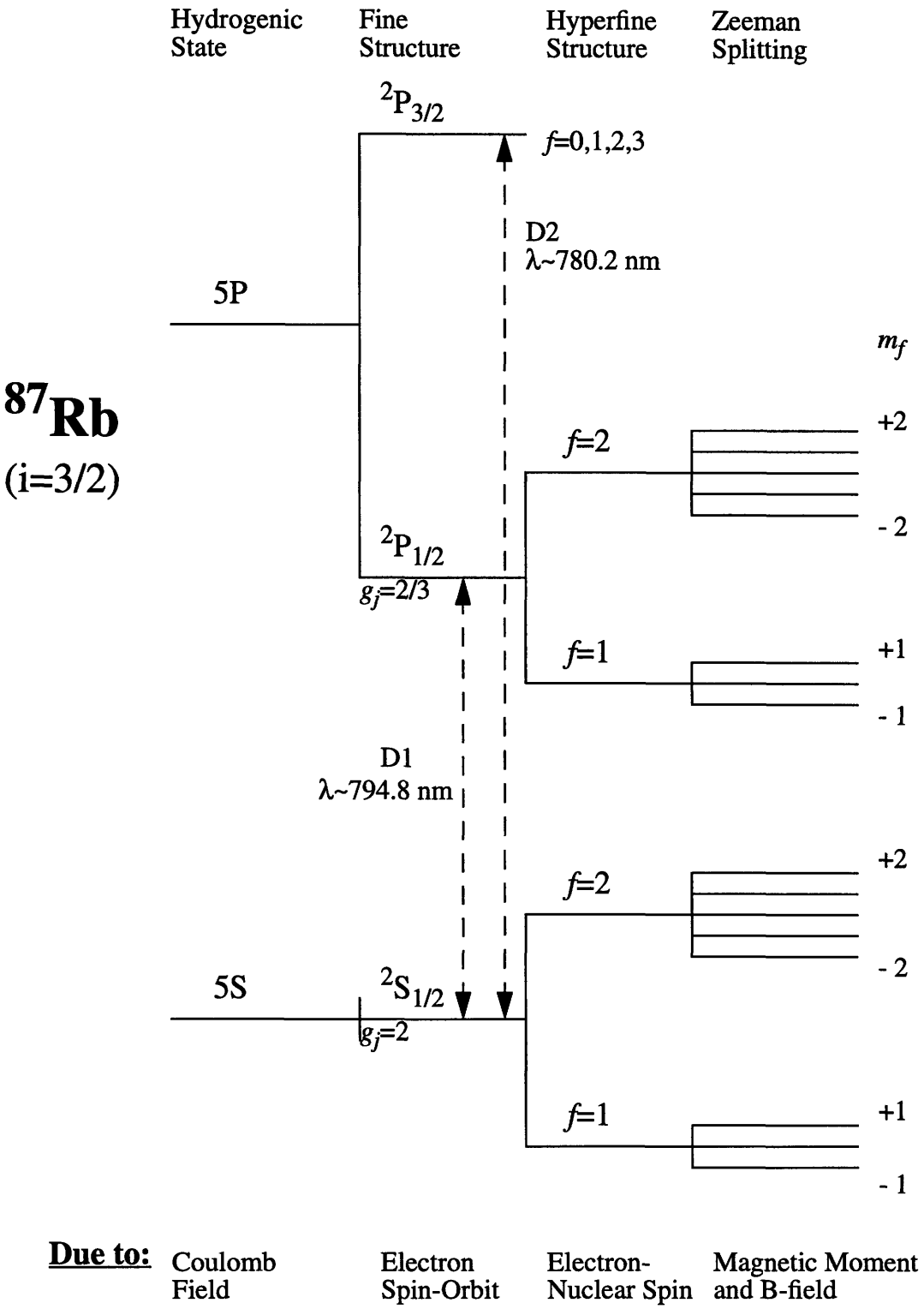


**Figure 3.2:** Schematic energy level diagram (not to scale) of $^{87}$Rb.

The **hydrogenic states** are due to the interaction between the valence electron charge and the coulomb field due to the nucleus and the screening electrons. We can write the basic Hamiltonian as

$$\hat{H} = \frac{\hat{p}^2}{2m} - \frac{e^2}{r}. \tag{3.6}$$

This interaction yields the principle quantum numbers and the orbital angular momentum quantum numbers. The energies are of the order $\Delta E \sim \alpha^2 mc^2$ where $\alpha = e^2/\hbar c \sim 1/137$ is the fine structure constant. Actually, since the energy dies off with $1/n^2$, n being the principle quantum number, the Bohr energies in rubidium are actually an order of magnitude smaller, $\Delta E \sim 1$ eV.

The **fine structure** comes from the coupling of the ***S*** and ***L*** of the valence electron. We ignore relativistic effects which are of the same order. The Hamiltonian contribution is

$$\hat{H}_{LS} = \hat{\mu} \cdot \left(\frac{\hat{p}}{mc} \times \hat{E}\right) = \frac{1}{m^2 c^2} \cdot \frac{1}{r} \cdot \frac{dV}{dr} (\hat{L} \cdot \hat{S}). \tag{3.7}$$

The standard notation of the state is ${}^{2s+1}l_j$. To add to the confusion, letters represent the values of $l$; $l = 0$ is represented by S (in spectroscopy, it is the sharp line), $l = 1$ is represented by P (the principle line). In the example of the rubidium levels seen in figures 3.1 and 3.2, there is a dual split in the ${}^2$P level. This is referred to as a "doublet", indicated in the notation by the superscript $2s+1 = 2$. The fine structure substates have an energy difference on the order of $\Delta E \sim \alpha^4 mc^2 \sim 10^{-3}$ eV.

The **hyperfine structure** arises from the interaction of the magnetic moments of the electrons and the nucleus. $\Delta E \sim (m/m_p)\alpha^4 mc^2 \sim 10^{-6}$ eV.

The **Zeeman splitting** described earlier in this section is due to an external magnetic field acting on the total magnetic moment of the atom. A strong external field that dominates over the fine structure coupling would cause nonlinear splitting.

### 3.1.3 Selection Rules

In this treatment, we only consider the electric dipole transition from a state |a⟩ to a state |a'⟩, assuming that the transition probabilities of other mechanisms are small in comparison. The Wigner-Eckart theorem [12] states that for angular momentum eigenstates, the matrix elements of tensor operators satisfy

$$\langle \alpha', f', m_f' | \hat{T}_q^{(k)} | \alpha, f, m_f \rangle = \langle f, k; m_f, q | f, k; f', m_f' \rangle \frac{\langle \alpha', f' || \hat{T}^{(k)} || \alpha, f \rangle}{\sqrt{2f+1}} \tag{3.8}$$

where $\alpha$ is a string of other relevant quantum numbers, $\langle f,\ k;\ m_f,\ q | f,\ k;\ f',\ m_f' \rangle$ is the Clebsch-Gordan coefficient, and $\langle \alpha', f' || T || \alpha, f \rangle$ is the reduced matrix element. In the case we are interested in, the tensor $T_q^{(k)}$ is the electric dipole moment operator. To understand what $k$ and $q$ are, we need a quantum understanding of light as a photon with an intrinsic angular moment of $1\hbar$. Thus $k = 1$, and $q$ is its projection in the atomic frame, having values of $\{-1, 0, +1\}$ corresponding to various polarizations of the light. From the Clebsch-Gordan coefficients, we obtain the following selection rules:

$$\Delta l = \pm 1 \tag{3.9}$$

$$\Delta f = 0, \pm 1 \tag{3.10}$$

$$\Delta m_f = q \tag{3.11}$$

The third selection rule is of particular interest because it shows that the transitions in the Zeeman sublevels are dictated by the polarization of the light. Linearly polarized light ($\pi$-polarized, corresponding to $q = 0$) will couple states with the same value of $m_f$, and circularly polarized light ($\sigma$, corresponding to $q = \pm 1$) will couple states where $\Delta m_f = \pm 1$ respectively.

## 3.2 The Λ System

### 3.2.1 Optical Pumping

Under thermal equilibrium conditions, the distribution of energy states in an ensemble of atoms is described by the Boltzmann distribution law [13]. For two energy states $E_1$ and

$E_2$, the ratio of atoms in those states $n_1/n_2$ is

$$\frac{n_1}{n_2} = e^{\left(\frac{E_2 - E_1}{k_B T}\right)} \tag{3.12}$$

where $k_B = 1.38 \times 10^{-16}$ erg•K$^{-1}$ is the Boltzmann constant. From this relation, we find that at room temperature, only one atom for every 10 kilograms of rubidium is in an excited state.

Optical pumping is a method in which the absorption of light leads to population distributions that differ from the Boltzmann distribution. An ideal picture of how this might work is shown below in figure 3.3. This model is of the $f = 1 \rightarrow f' = 1$ transitions in $^{87}$Rb (specifically, this is the $5^2S_{1/2}$, $f$=1 → $5^2P_{1/2}$, $f$=1 transition). These transitions are allowable since they satisfy the selection rules in equations (3.9) and (3.10). A forward pump beam $\sigma_+$ polarized and a backward pump beam $\sigma_-$ polarized excite the atoms.

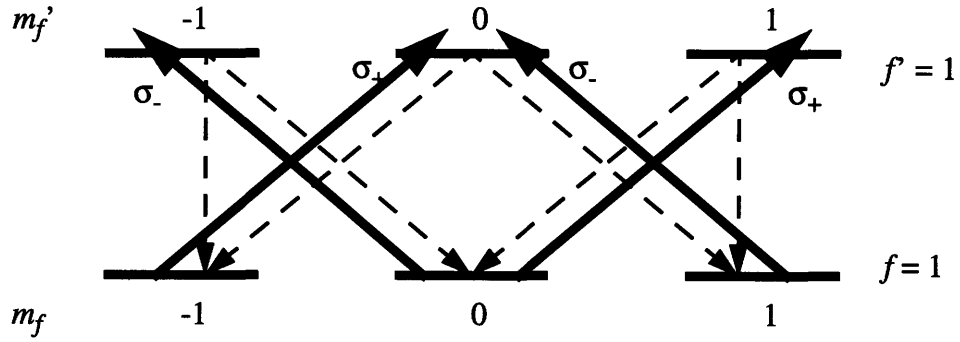


**Figure 3.3:** Optical pumping between Zeeman states. Solid lines are transitions induced by pump beams and dashed lines are spontaneous emissions.

Selection rule (3.11) dictates which transitions are caused by the polarized pump beams. The Clebsch-Gordan coefficients also indicate that $m_f = 0 \rightarrow m_f' = 0$ is invalid. So after a few cycles, the electrons are depleted from the $m_f = 0$ state and the $m_f' = \pm 1$ states. The resulting system is equivalent to a three-level Raman system as illustrated in figure 3.4. Because of its schematic shape, this configuration is also known as a $\Lambda$ system.

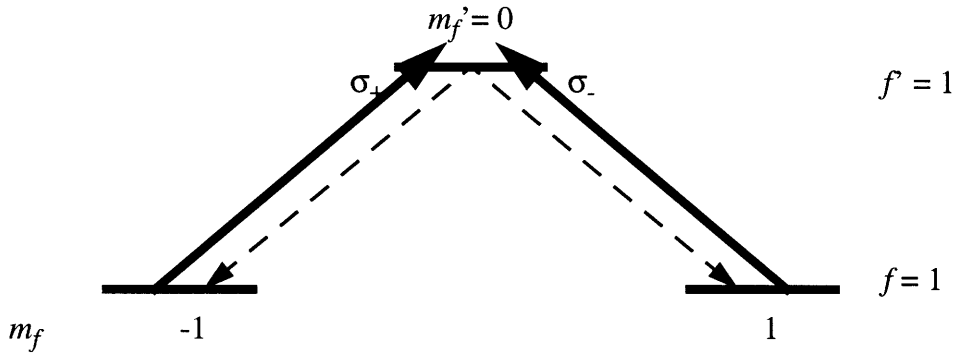


**Figure 3.4:** The Λ system.

### 3.2.2 Coherent Population Trapping

Coherent population trapping (CPT) is an optical pumping process that involves a superposition of the atom's electronic states. To understand how this works, consider the system in figure 3.5. The four beams involved with OPC, with their propagation and polarization directions and their detuning, are shown interacting with the Λ system in figure 3.5(a). Figure 3.5(b) shows a single Λ system consisting of two ground states $|a\rangle$ and $|b\rangle$ with the excited state $|e\rangle$. The transition frequency coupling a ground state to the excited state is $\omega_i$, and the associated Rabi frequency is

$$\Omega_i = \frac{\vec{d}_i \cdot \vec{E}_i}{\hbar}, i \in \{1, 2\} \tag{3.13}$$

where $d$ is the electric dipole moment of the atom and $E$ is the applied electric field due to the laser beam. The Rabi frequency is expressed as a complex value which includes an amplitude and a phase factor. Optical pumping brings the atoms into a superposition of the ground states:

$$|- \rangle = \frac{1}{\sqrt{\Omega_1^2 + \Omega_2^2}}(\Omega_2|a\rangle - \Omega_1|b\rangle) \tag{3.14}$$

This state is known as the dark state because it is transparent to the transition beams. The following simple calculation shows that it is decoupled from the excited state:

$$\langle e|\hat{H}|- \rangle = \frac{1}{\sqrt{\Omega_1^2+\Omega_2^2}}\langle e|\hat{H}\{\Omega_2|a\rangle - \Omega_1|b\rangle\}$$

$$= \frac{1}{\sqrt{\Omega_1^2+\Omega_2^2}}\{\Omega_2\langle e|\hat{H}|a\rangle - \Omega_1\langle e|\hat{H}|b\rangle\}$$

$$= \frac{1}{\sqrt{\Omega_1^2+\Omega_2^2}}(\Omega_2\Omega_1 - \Omega_1\Omega_2)$$

$$= 0 \qquad . \tag{3.15}$$

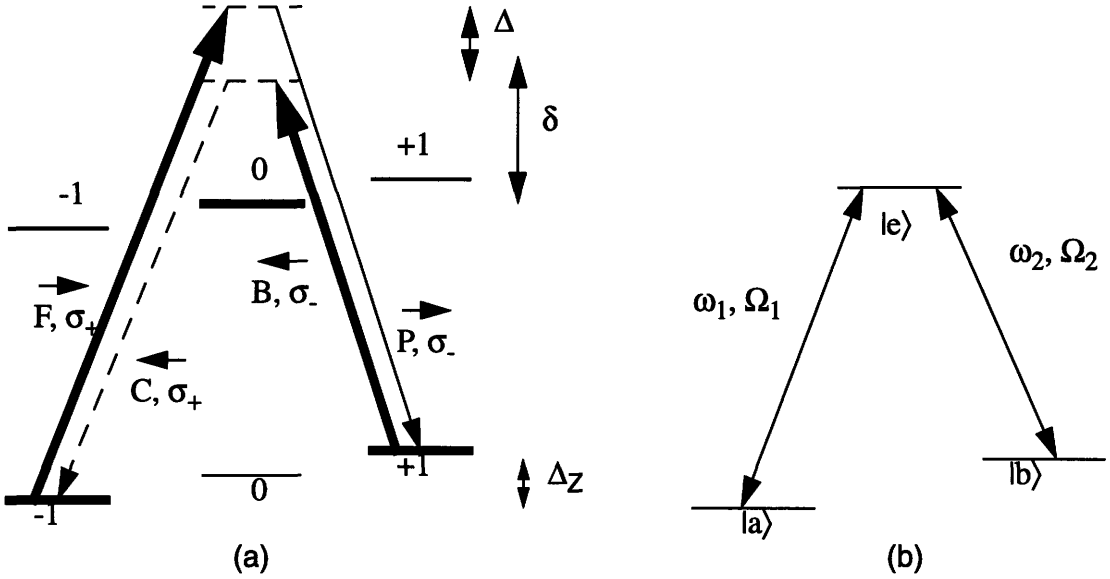


**Figure 3.5:** The Λ configuration for CPT (a) illustration of the four-wave mixing interaction, (b) Coupling of the states.

We can draw a diagram with new basis states: instead of |a⟩ and |b⟩, use |-⟩ and |+⟩, where |-⟩ and |+⟩ are orthogonal and |+⟩ is expressed by

$$| + \rangle = \frac{1}{\sqrt{\Omega_1^2+\Omega_2^2}}(\Omega_2|a\rangle + \Omega_1|b\rangle)\,. \tag{3.16}$$

This is illustrated in figure 3.6. So atoms will be pumped from the bright state |+⟩ into the excited state. From there, the atoms, through emission, can enter the dark state |-⟩ where they are trapped.

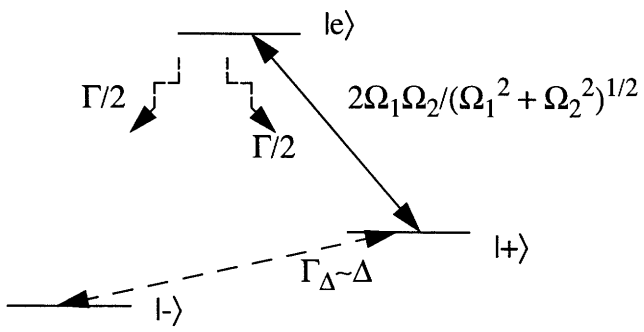


**Figure 3.6:** CPT in the dark state. Detuning in the ground states cause some coupling to occur between |-⟩ and |+⟩.

Referring back to figure 3.5(a), we can see how CPT is applied to OPC. For this case, we see that the forward pump (F) and the probe (P) form one Λ system, while the backward pump (B) and the conjugate (C) form another. From equation (3.14) the dark states are

$$|-\rangle_{FP} = \frac{1}{\sqrt{\Omega_F^2+\Omega_P^2}}(\Omega_P e^{i(\vec{k}_P\cdot\vec{r})}|a\rangle - \Omega_F e^{i(\vec{k}_F\cdot\vec{r})}|b\rangle) \tag{3.17}$$

$$|-\rangle_{BC} = \frac{1}{\sqrt{\Omega_B^2+\Omega_C^2}}(\Omega_B e^{i(\vec{k}_B\cdot\vec{r})}|a\rangle - \Omega_C e^{i(\vec{k}_C\cdot\vec{r})}|b\rangle) \tag{3.18}$$

For simplicity in the model, we assume that F and P saturate the two-photon transition, and that B and C are weak [6]. Now only the $|-\rangle_{FP}$ dark state needs to be considered; the system is only transparent to F and P. When every atom reaches the dark state, the ground state coherence is expressed by the atomic density matrix element

$$\rho_{ab} = -\frac{\Omega_P\Omega_F^*}{|\Omega_P|^2+|\Omega_F|^2}e^{i\phi}; \tag{3.19}$$

$$\phi \equiv (\vec{k}_F - \vec{k}_P)\cdot\vec{r}. \tag{3.20}$$

This result shows that CPT writes a purely sinusoidal grating in the coherence between the two ground states. The main advantage of this method is that saturation of the system

corresponds to optical pumping into the dark state. Consequently, low powers are sufficient to saturate the two-photon transition and to write the grating from which the backward beam can scatter. We can determine the threshold power by equating the transition rate due to dephasing between the ground states ($\Gamma_\Delta$) to the rate of optical pumping which is given by

$$\Gamma\rho_{ee} = \frac{\Omega^2}{\Gamma}; \tag{3.21}$$

$$\Omega \equiv \sqrt{|\Omega_F|^2 + |\Omega_S|^2}\ . \tag{3.22}$$

However, the optical pumping rate in the Raman system is slower than the response time of the two-level atomic system. Yet as shown in table 1.1, the system is still quite fast.

A few interesting points need to be considered in the case of the degenerate system (detuning $\Delta = 0$, $\omega_1 = \omega_2$). Since the dark state and the bright state are completely uncoupled, all of the atoms are trapped in the dark state. At this point, the system becomes completely transparent to all the beams (which are now all the same frequency, and thus contribute to the same dark state). This is the Raman dip in figure 3.7, which can be plotted from the relation between the population and detuning [14]:

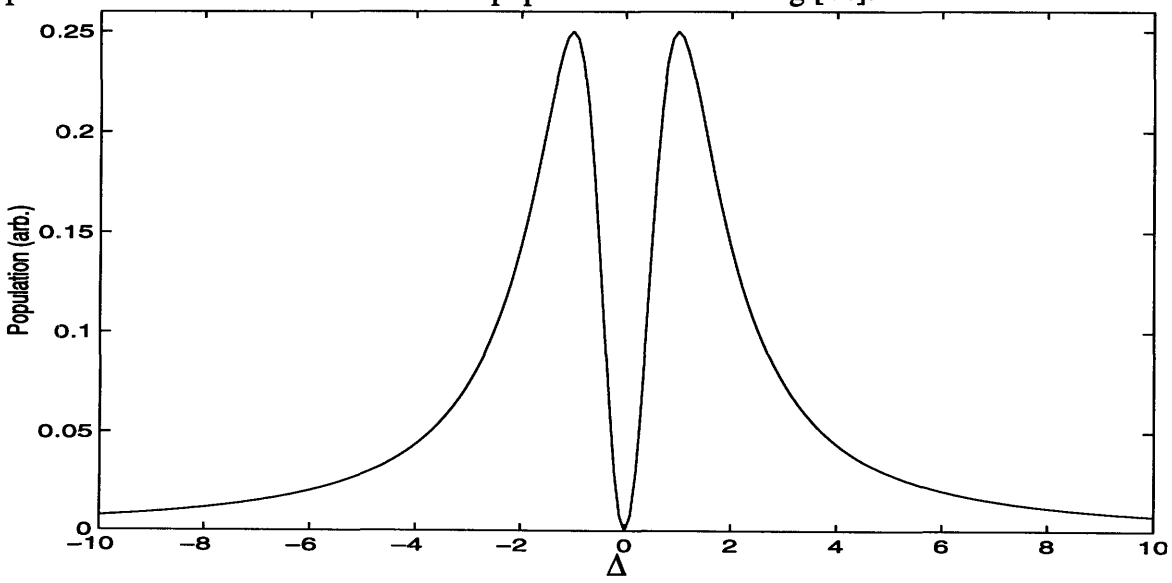


**Figure 3.7:** Raman dip where $\Omega = \Gamma$, $\Delta$ in units of $\Gamma$.

$$\rho_{ee} = \frac{\Omega^2\Delta^2}{\Omega^4 + \Omega^2\Delta^2 + \Delta^2\Gamma^2 + 4\delta^2\Delta^2 + \Delta^4} \tag{3.23}$$

Obviously, this transparency of the system contributes to the plausibility argument explaining the lower reflectivity and gain of a degenerate Raman PCM, compared with the nondegenerate case. The fact that there is any conjugate reflectivity at all comes in part from the counterpropagation of the pump beams. This geometry assigns a value of momentum to each of the states. If the excited state $|e\rangle$ has a momentum $\boldsymbol{p}_e = u$, the forward beam has a momentum of $\hbar k$, and the backward beam has a momentum of $-\hbar k$, then $|a\rangle$ will have a moment $\boldsymbol{p}_a = u - \hbar k$ and $|b\rangle$ will have a momentum $\boldsymbol{p}_b = u + \hbar k$. Thus the dark state is

$$|- \rangle = \frac{1}{\sqrt{2}}(|a, \vec{p}_a\rangle - |b, \vec{p}_b\rangle) \tag{3.24}$$

which is velocity selective, transparent only to certain velocity groups.

We can also deduce the existence of a theoretical limit for the conjugate reflectivity in the nondegenerate case from the dark state relations in (3.17) and (3.18). Since the Rabi frequencies depend on the field intensities of the beams, we can estimate that the gain will diminish as the conjugate intensity approaches $I_C \sim I_F I_B / I_P$. At this point, both the dark states $|-\rangle_{FP}$ and $|-\rangle_{BC}$ approach each other, increasing the transparency of the system.

### 3.2.3 Angular Momentum Representation of the Dark State

A model to help visualize the coherence grating can be found in drawing angular momentum vectors [2]. Consider the $f = 1$ to $f' = 1$ transition detailed in section 3.2.1. We arbitrarily define the lab coordinate frame such that $z$ is the axis of quantization and the propagation vectors of the forward and probe beams are

$$\vec{k}_F = k(\hat{x}\sin\alpha + \hat{z}\cos\alpha) \tag{3.25}$$

$$\vec{k}_P = k(-\hat{x}\sin\alpha + \hat{z}\cos\alpha) \tag{3.26}$$

where $2\alpha$ is the small angle between the two beams. These beams propagate close to the $z$-

direction and form a grating in the $x$-direction. For this treatment, we will label the magnetic quantum numbers $m_z$ rather than $m_f$ in order to recognize the direction of quantization. The interpretation of the $m_z$ states is illustrated in figure 3.8. The vector has a length of $[f(f+1)]^{1/2}\hbar$ and precesses around the $z$-axis. The value of $m_z$ is the vector's projection in units of $\hbar$ onto the $z$-axis.

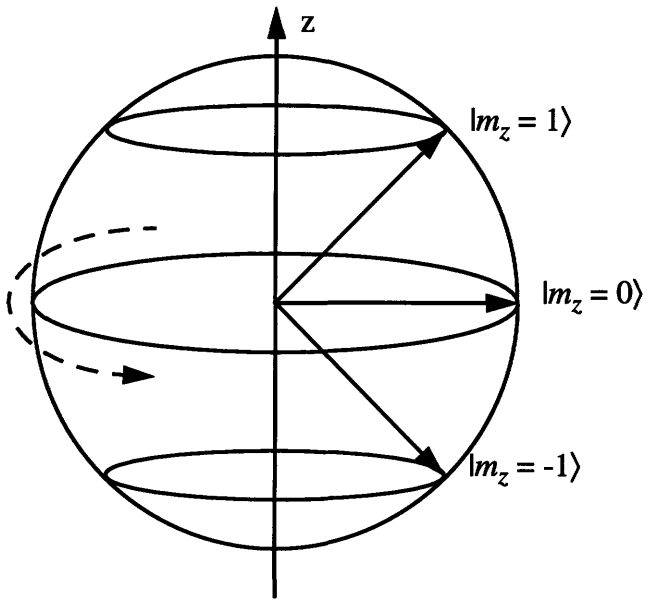


**Figure 3.8:** Angular momentum representation of the Zeeman sublevels.

From equation (3.17), the dark state is a superposition of the $|m_z = 1\rangle$ and the $|m_z = -1\rangle$ states.

$$|- \rangle = \frac{e^{i(\vec{k}_P \cdot \vec{r})}}{\sqrt{2}}(|1\rangle - e^{i\phi}|-1\rangle) \tag{3.27}$$

where $\phi$ is defined in equation (3.20). Since $(k_F - k_P)$ is in the $x$-direction, $\phi$ can be simplified to be $\phi(x) = (k_F - k_P) \bullet x = \Delta kx$. We can transform coordinates such that the dark state $|-\rangle = |m_{z'} = 0\rangle$, where $|m_{z'} = 0\rangle$ is analogous to $|m_z = 0\rangle$ except that it precesses around the $z$'-axis. The $z$'-axis will always be orthogonal to the $z$-axis, with its orientation on the $x$-$y$ plane dependent on the value of $\phi$.

# Chapter 4

# The Experiment

## 4.1 Overview

A schematic of the OPC experimental setup is found in figure 4.1. Excluded from the figure are lenses used to size the beams, beamsplitters and choppers used for diagnostics and measurements, as well as all the extra mirrors used to configure the real system.

All of the beams come from a single frequency stabilized titanium-sapphire laser pumped by an argon dye laser. This ensures that the frequencies of the beams are degenerate. The individual beams are separated using beamsplitters. The frequency of the ti-sapphire laser is locked to the $D_1$ transition line of rubidium, which has a wavelength of approximately 794.98 nm (refer to figures 3.1 and 3.2). The output power is maintained at around 1 W.

Since orthogonal components of a beam's polarization reflect off of mirrors differently (assuming non-normal incidence), a large number of mirrors in the setup will cause the beam to become elliptically polarized. To address this concern, $\lambda/2$ plates, which rotate a beam's polarization, are used in conjunction with polarized beamsplitting cubes. This scheme also effectively controls the power levels of the individual beams. The beamsplitting cubes ensure that the beams are linearly polarized before reaching the $\lambda/4$ plates. $\lambda/4$ plates convert linearly polarized light into circularly polarized light, which is what we desire for the interaction in the rubidium cell.

Telescoping lenses focus the pump beams to a FWHM radius of around 1 mm at the center of the rubidium cell. The probe beam is focused to a FWHM radius of approximately 0.7 mm. Similar to the analysis of previous chapters, the pump beams are roughly counterpropagating, yet with a small angle between them. Two mirrors placed 1 m

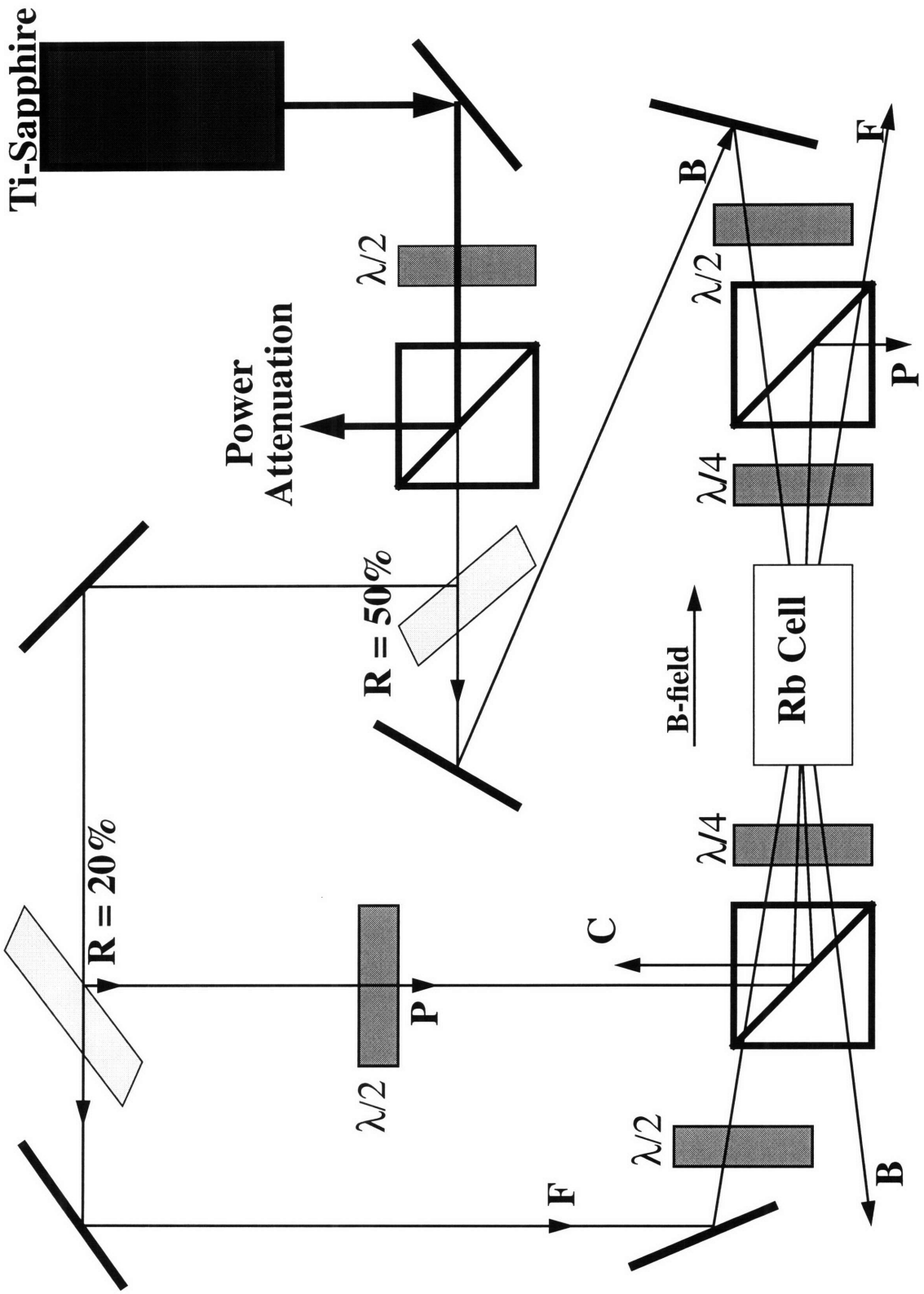


**Figure 4.1:** Schematic of the experimental setup for OPC.

apart symmetrically on either side of the cell are a gauge for rough alignment. The positioning of the beams on these mirrors form a square, with sides of length 5 mm. This geometry is shown in figure 4.2 below.

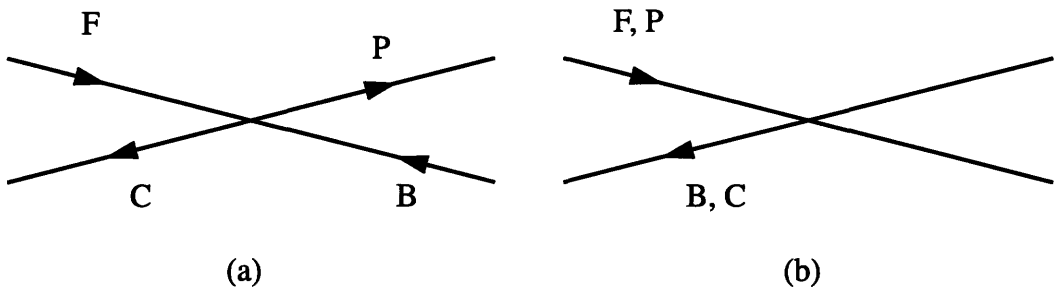


**Figure 4.2:** Geometry of the beams (a) side view (b) top view.

## 4.2 The Elements

A number of subsystems involved with the experiment are described in this section.

### 4.2.1 Saturated Absorption

In order to lock the ti-sapphire laser's frequency to the desired transition, a saturated absorption setup is used. As light passes through the atomic vapor, photons near the transition frequencies are absorbed as they excite the atoms. Due to the Doppler effect, atoms moving at different velocities see different photon frequencies. This scheme takes both of these properties into account to detect the atomic transitions in the Doppler profile.

The setup is illustrated in figure 4.3. Two weak beams are separated out with a piece of thick glass. One of these beams measures the Doppler profile. The other beam (call it the probe, not to be confused with the probe beam of the OPC setup) travels along the path of a counterpropagating strong beam that excites the atoms in the velocity group that sees the beam shifted to the absorption frequency. Since the beams have degenerate frequencies, it follows that the probe beam excites the atoms with the opposite velocity. When the laser frequency approaches an absorption line, the relevant atoms in question have zero

velocity. Thus the strong beam excites these atoms, saturating the absorption spectrum, making these atoms transparent to the probe beam. This results in peaks in the beam's intensity measurement vs. the laser frequency. These peaks are made clearer when the measurement of the unsaturated beam is subtracted from the measurement of the probe beam.

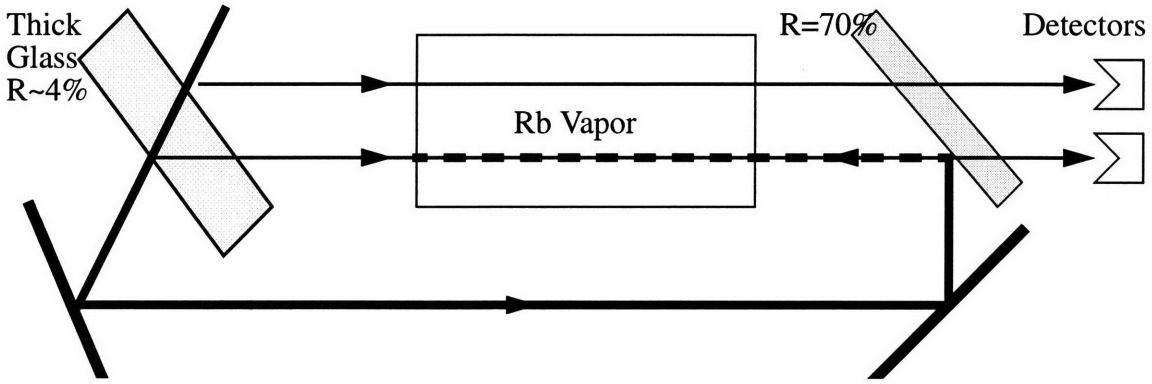


**Figure 4.3:** Saturation absorption setup.

Experimentally, peaks are found at frequencies that are not atomic transitions. For a laser frequency $\nu_L$, consider the situation where the probe and the strong beam interact with the same velocity group of atoms, each hitting the frequency of a different transition. Again, the strong beam will excite these atoms, causing the probe to see less absorption. These frequencies will be $\nu_1 = \nu_L(1 - v/c)$, $\nu_2 = \nu_L(1 + v/c)$. Playing with these equations, we find that this case occurs when $\nu_L = (\nu_1 + \nu_2)/2$. So peaks occur when the laser frequency is exactly between two absorption lines. These peaks are known as crossovers.

### 4.2.2 Rubidium Cell

For rubidium to be useful as an OPC medium, several issues are important to consider. Rubidium in the solid state does not behave as ideally as the model presented in chapter 3. In an atomic vapor, each atom behaves more like a nearly isolated system. Rubidium is also a highly reactive element, igniting when in contact with air, exploding when in contact with water. A good vacuum system that meets the following conditions is needed:

☞ The cell is easy to heat

☞ The cell offers optical access to its contents

☞ The rubidium vapor in the cell does not condense on the cell walls, and thus does not also, block optical access.

A heat-pipe oven shown in figure 4.4 is the solution we use. The oven is essentially crossed pipes soldered together. The base of the cross contains the rubidium reservoir, while the ends of the arms have windows to allow the optical beams to enter. The vacuum is obtained with a single mechanical pump that brings the cell down to a pressure of around 10-15 microns of mercury, on the order of $10^{-5}$ atm.

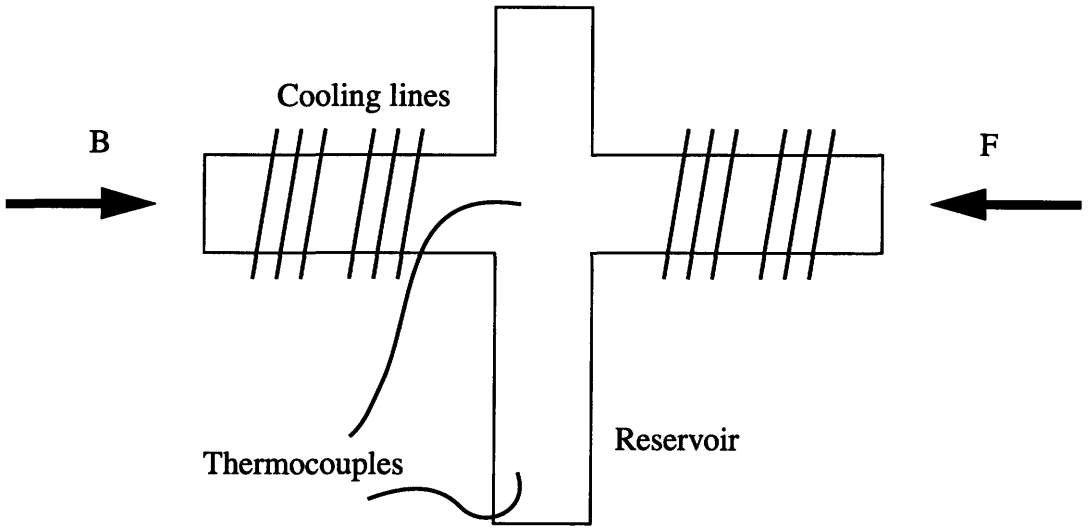


**Figure 4.4:** Heat-pipe oven.

Two heating systems are applied to the cross. One is for the reservoir, which is accomplished with the use of heating tape. The other is for the interaction region at the intersection of the cross. Three layers of heating coils are placed at the intersection. Thermocouples are placed at the areas of interest to monitor the temperature. Cooling water pipes are set on both arms of the cell. This helps prevent the rubidium vapor from leaving the interaction region and condensing on the windows.

To obtain a controlled magnetic field to separate the Zeeman sublevels, Helmholtz coils are placed around the arms of the cell. These are a pair of identical circular coils of 95 turns of copper wire, spaced equidistant (about 4") from the center of the cross. For every Ampere of current applied on the coils, they produce a B-field of approximately 8.33 Gauss at the interaction region. In order to protect the atomic system from potential sources of unwanted magnetic fields, the cross is enclosed in a metal box. Also, the heating coils are accomplished with twisted pairs of nichrome and copper to minimize their magnetic field generation.

## 4.3 The Phase Conjugate Resonator

In order to realize the resonator cavity, the conjugate beam must be made to fall onto the path of the probe beam and reenter the rubidium cell (the PCM). The probe beam generated from the ti-sapphire laser is used to help align the conjugate, but when the system is properly aligned and the reflectivity of the PCM is high, the probe beam is no longer needed. The spontaneous emissions are amplified and yields lasing.

The first configuration in figure 4.5 is the ring laser. Attempts to make a standing wave cavity by aligning the pump beams to counterpropagate exactly have so far not been very successful because the gain of the system falls below unity. However, figures 4.6 and 4.7 demonstrate an attempt to simulate the standing wave cavity. The $\lambda/4$ and $\lambda/2$ plates in the path of the probe and the conjugate adjust the polarization of the beams so that they follow the correct path through the beamsplitting cubes.

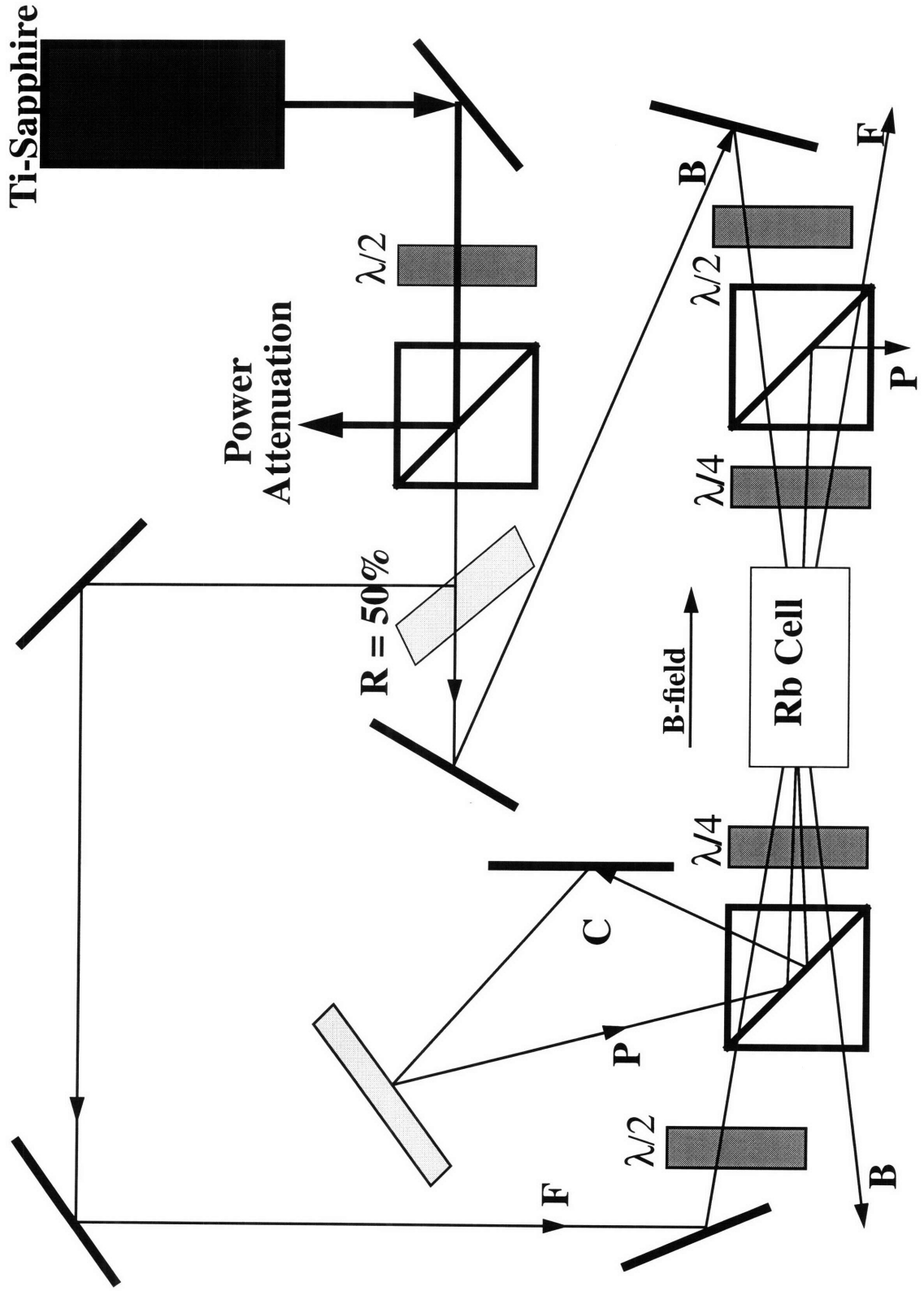


**Figure 4.5:** The ring laser cavity.

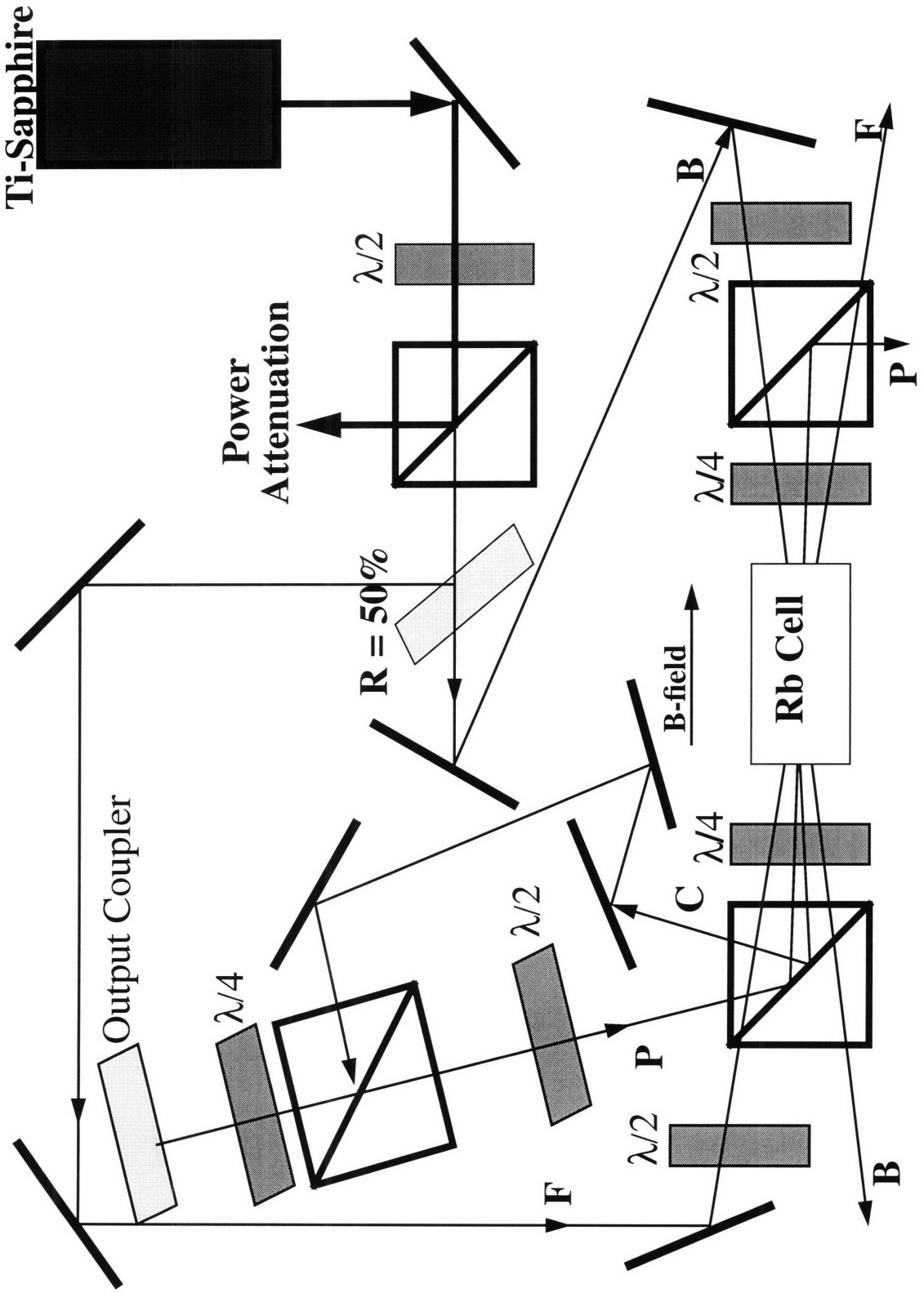


**Figure 4.6:** Effective standing wave cavity.

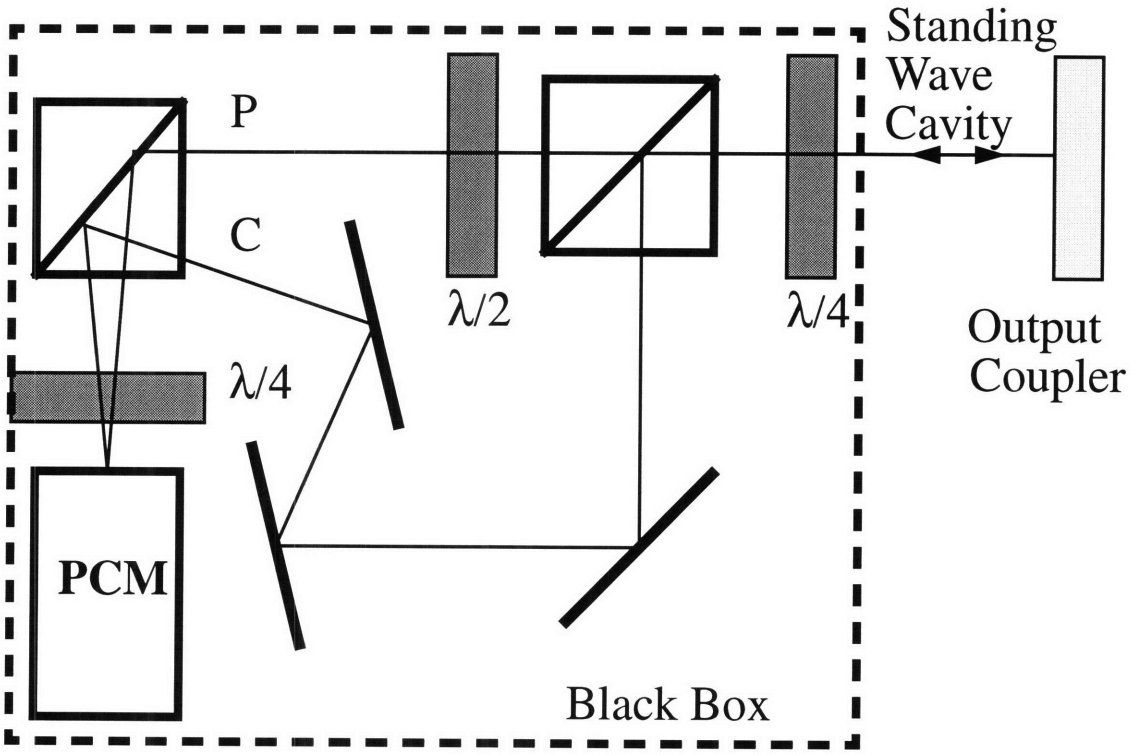


**Figure 4.7:** A cleaner picture of the standing wave cavity.

# Chapter 5

# Results

## 5.1 Saturated Absorption

Figure 5.1 shows the scan obtained from the saturation absorption setup and the corresponding conjugate output. The Ti-sapphire laser is set at the $D_1$ transition. The probe and the pump beams have degenerate frequencies. The zero frequency point is arbitrarily set at the peak from the $5^2S_{1/2}$, $f$=2 → $5^2P_{1/2}$, $f'$=1 transition of $^{87}$Rb. This transition yields the highest gain in part due to the existence of three Λ systems in the Zeeman sublevels ($m_f$ = -2 to 0, -1 to 1, 0 to 2).

However, upon close examination of the results, the maximum conjugate output occurs when the laser frequency is blue-shifted from the transition frequency. This supports the prediction in section 3.2.2 concerning the velocity selectiveness of the system. Whereas in the nondegenerate case, the greatest conjugate output occurs exactly on the transition frequency and the zero velocity atoms make the greatest contribution, here in the degenerate case, the greatest contribution comes from atoms in a non-zero velocity group.

## 5.2 The Phase Conjugate Mirror

The results recorded for this system were obtained under the following conditions:

- ☞ Ti-sapphire laser tuned to the frequency with the optimal conjugate gain;
- ☞ Forward pump power: 84 mW;
- ☞ Backward pump power: 24 mW;
- ☞ Temperature of the reservoir: 490 K;
- ☞ Temperature of the interaction region: 415 K.

Previous work demonstrates that the conjugate beam's polarization follows the theoretical prediction [15]. The amount of conjugate reflected in the beamsplitting cube (corresponding to $\sigma_+$ polarization) is 400 times that transmitted in the beamsplitting cube (corresponding to $\sigma_-$ polarization). Thus all measurements are of the $\sigma_+$ component. Figure 5.2 plots the reflectivity of the PCM with respect to the incident probe power. At low powers, we obtain a reflectivity of around 40. The transmitted probe beam has similar gain characteristics. A stable conjugate beam is observed at some of the other transitions as well.

Figure 5.3 shows the effects of an applied magnetic field inducing a Zeeman shift. The resulting line is narrow; the full width at half maximum (FWHM) is approximately 1 MHz compared to 2.4 MHz in the nondegenerate case [2,15]. This is well below the natural linewidth of 5.8 MHz. To estimate the response time of the system, we can take advantage of our knowledge of the optical pumping rate in equation (3.21) and the coupling of the ground states due to detuning. The response time comes out to be $\tau = 1/2\pi \bullet$FWHM. The response time of this system is around 160 ns. This is still relatively fast.

Figure 5.4 demonstrates the dependence of the conjugate on the backward pump polarization. A $\lambda/2$ plate placed directly before the $\lambda/4$ plate controls the polarization. The backward beam changes from $\sigma_-$ to $\sigma_+$ polarization when the $\lambda/2$ plate is rotated 45° in either direction. Consistent with predictions and previous work, the conjugate beam does not form when the backward pump is incorrectly polarized.

## 5.3 The Ring Laser

The following are the conditions under which the results for this system were obtained:

- ☞ Ti-sapphire laser tuned to the frequency with the optimal conjugate gain;
- ☞ Forward pump power: 162 mW;

☞ Backward pump power: 91 mW;

☞ Temperature of the reservoir: 481 K;

☞ Temperature of the interaction region: 415 K.

There are two places where we observe the output of this laser system: one is along the path of the conjugate beam using a 98% beamsplitter as the output coupler, the other is along the path of the transmitted probe, the PCM itself being the output coupler. Both have a similar dependence on frequency. The conjugate path output power is around 0.02 mW, while the probe path output power is around 1 mW. Taking account of loss in the system due to other factors, we can estimate the internal intensities to be approximately 0.85 mW for the incident beam and 1 mW for the reflected. This indicates a gain in the PCM of around 1.2. Extra scattering from the pump beams obscures some of the results. This problem is resolved by making a separate measurement with just the noise, then subtracting the result from the measurement of the total output.

Figure 5.5 shows the measured output and noise vs. the laser frequency shift. The saturated absorption signal is also provided for comparison. Figure 5.6 subtracts out the noise to give only the laser cavity output. Again, note that the lasing occurs at a frequency blue-shifted from the $f=2 \rightarrow f'=1$ transition line. However, unlike the case of the PCM where a stable conjugate exists for other transitions, the $f=2 \rightarrow f'=1$ transition is the *only* line where lasing exists.

The threshold of this laser system demands higher power levels than the simple PCM. Because of this higher threshold, we expect the line from the magnetic field scan to be narrower (since the lower, wider parts of the line are cut off). Figure 5.7 measures the effect of a Zeeman shift on the system. As expected, the line is very narrow with a FWHM of around 0.6 MHz. Figure 5.8 shows the dependence of the laser cavity output on the backward pump's polarization. Whereas the PCM would still produce a conjugate beam

when the λ/2 plate is rotated 23° in either direction, the resonator will only lase if the λ/2 plate is rotated less than 3° in either direction.

## 5.4 The Effective Standing Wave Cavity

Measurements were taken under the following conditions:

- ☞ Ti-sapphire laser tuned to the frequency with the optimal conjugate gain;
- ☞ Forward pump power: 125 mW;
- ☞ Backward pump power: 84 mW;
- ☞ Temperature of the reservoir: 481 K;
- ☞ Temperature of the interaction region: 415 K.

Again, we made the same measurements as for the ring laser. The results which are documented in figures 5.9-5.12 are similar to those of the previous configuration. Unfortunately, tests indicate that this configuration has not been working like a standing wave cavity as hoped. Tests involving blocking the beams at several places indicate that lasing may have come from the beams following paths different from the prediction.

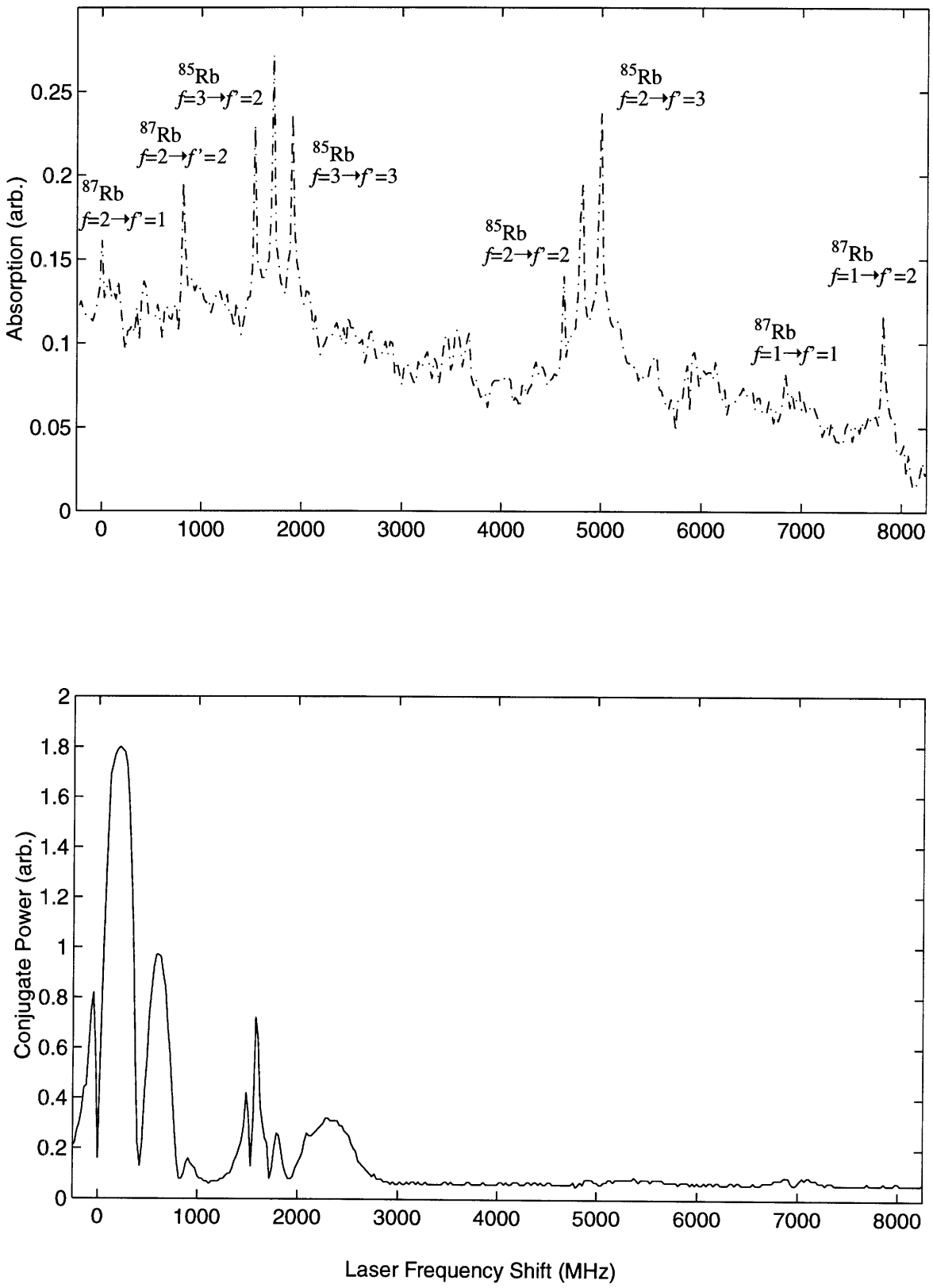


**Figure 5.1:** Rb $D_1$ absorption lines and conjugate power vs. frequency. The frequency shift is arbitrarily zeroed at the $f$=2 → $f'$=1 transition.

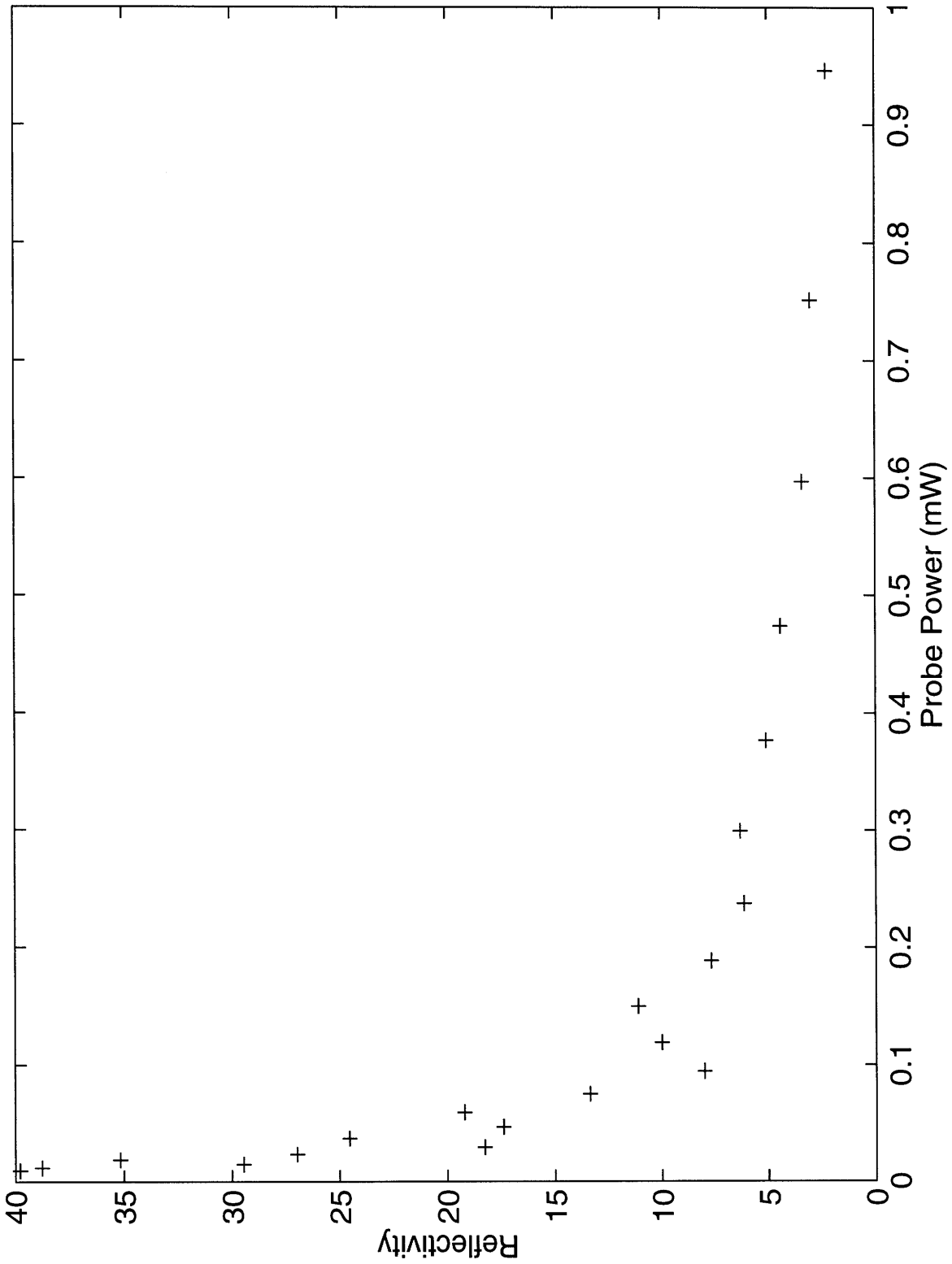


**Figure 5.2:** Reflectivity of the PCM.

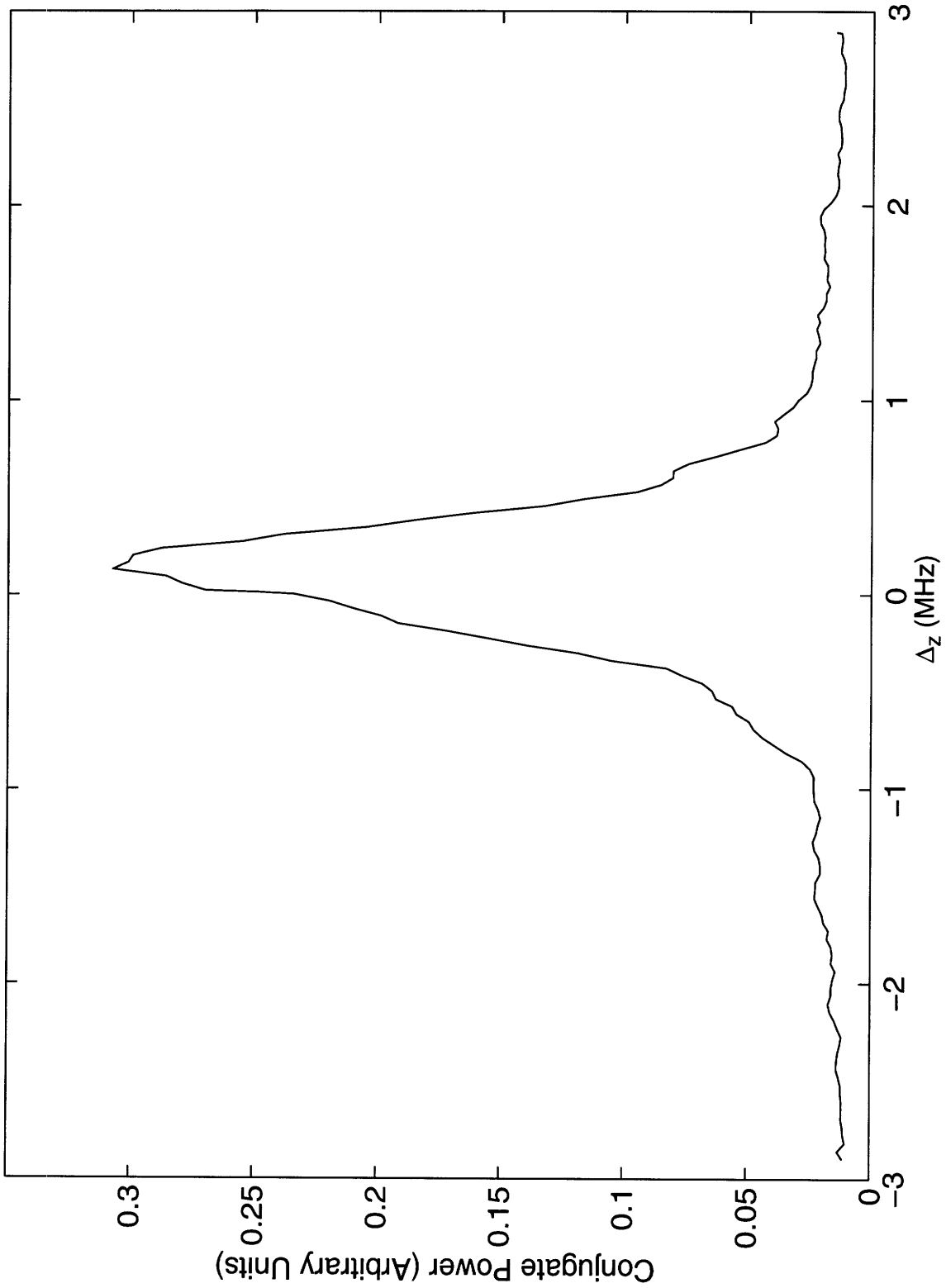


**Figure 5.3:** Dependence of the conjugate power on the magnetic field.

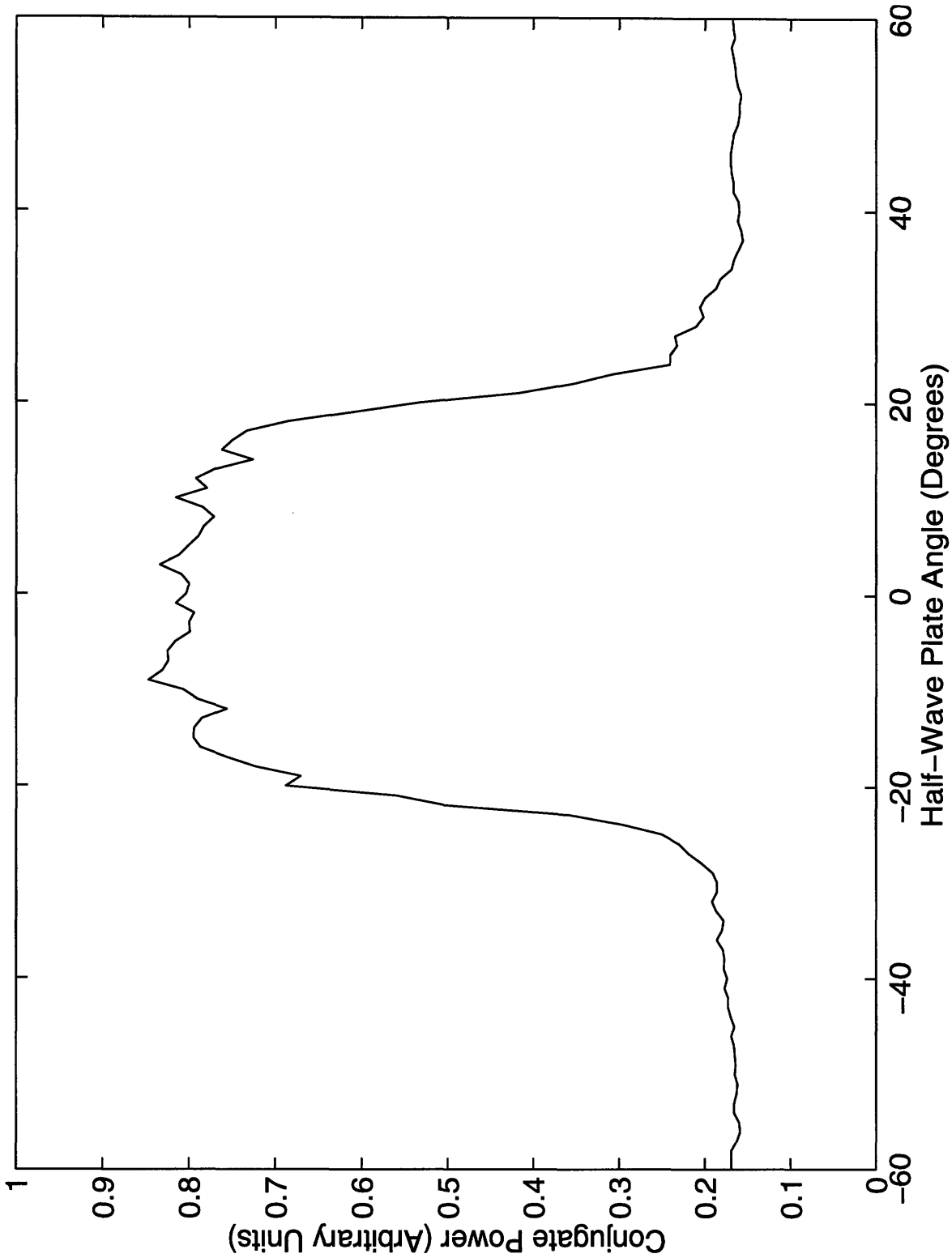


**Figure 5.4:** Dependence of the conjugate power on the polarization of the backward pump.

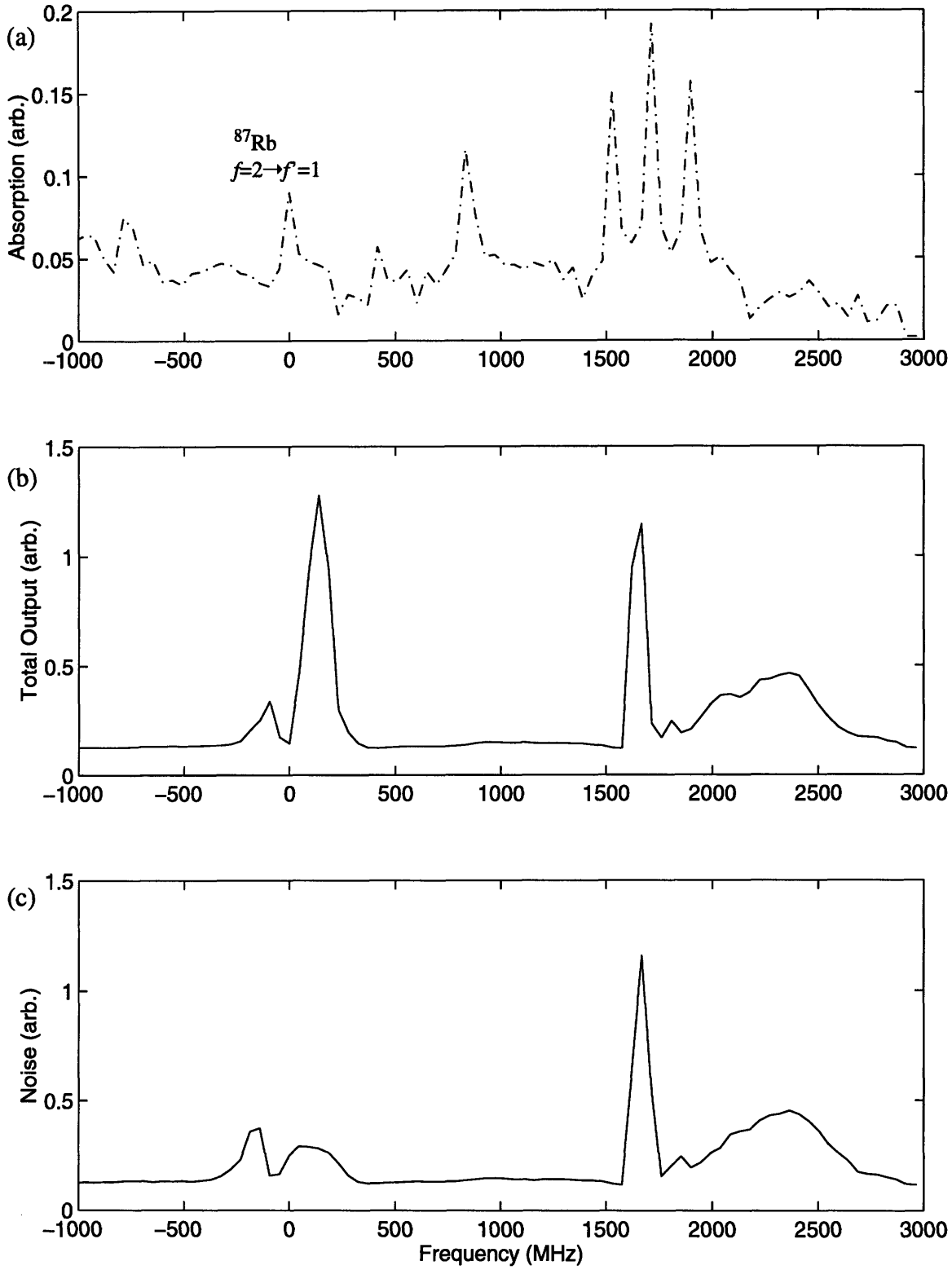


**Figure 5.5:** Dependence of the output of the ring laser cavity on frequency. (a) is the saturated absorption signal, (b) is the total output, (c) is the noise output. The units are arbitrary.

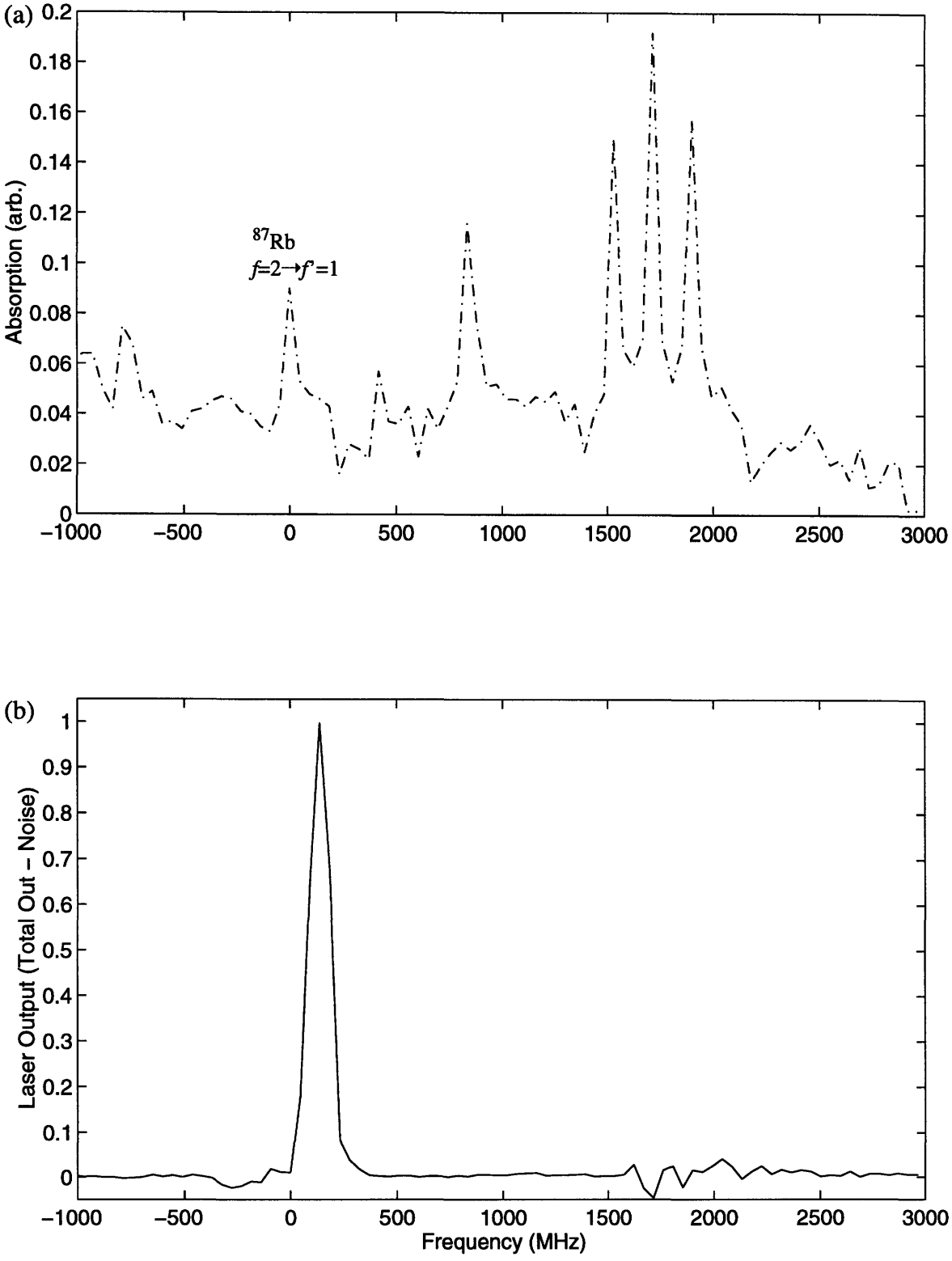


**Figure 5.6:** The difference of the total ring cavity output and the noise output. (a) is the saturated absorption signal, (b) is the derived output. The units are arbitrary.

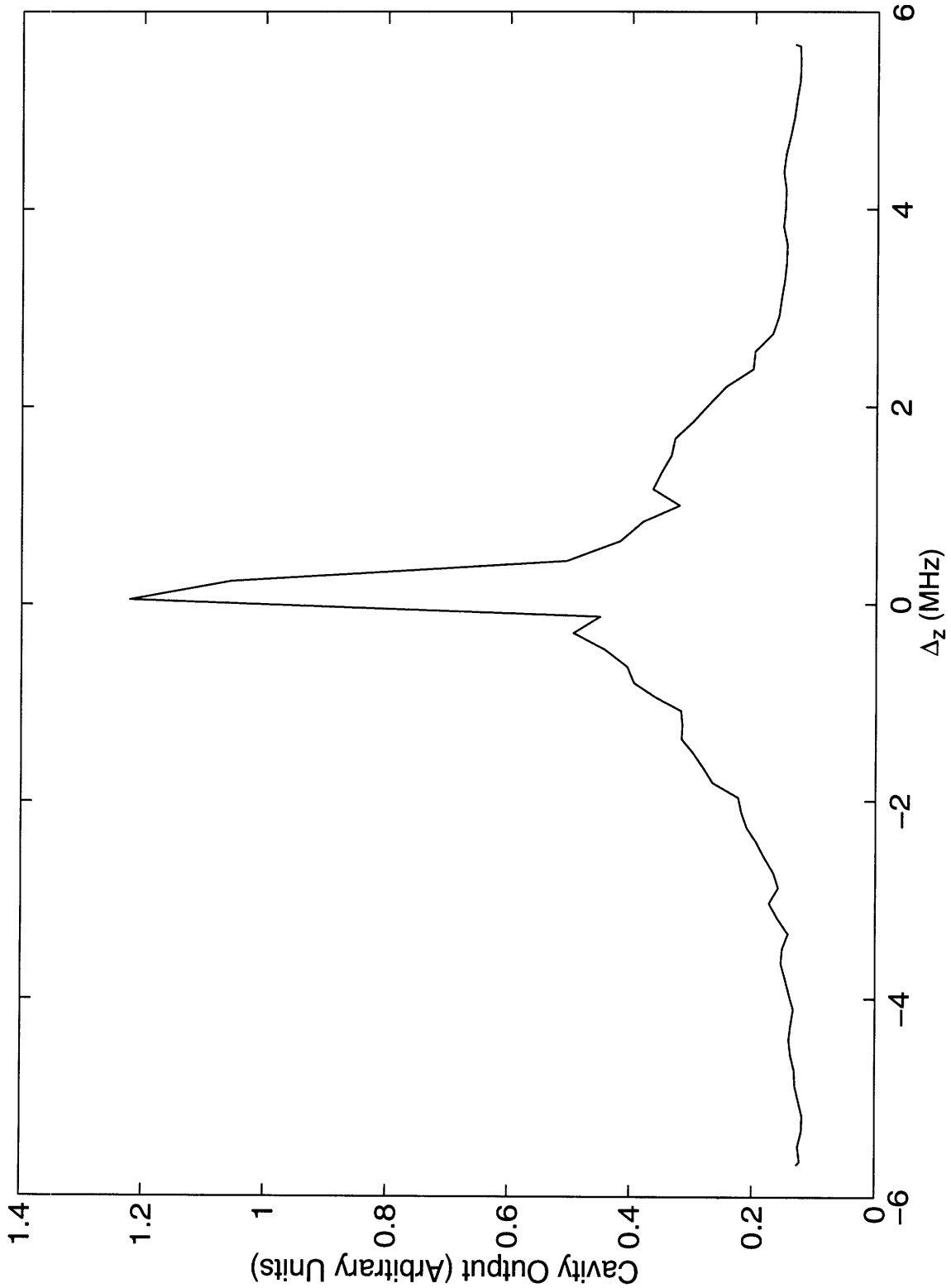


**Figure 5.7:** Dependence of the ring laser cavity output on magnetic field.

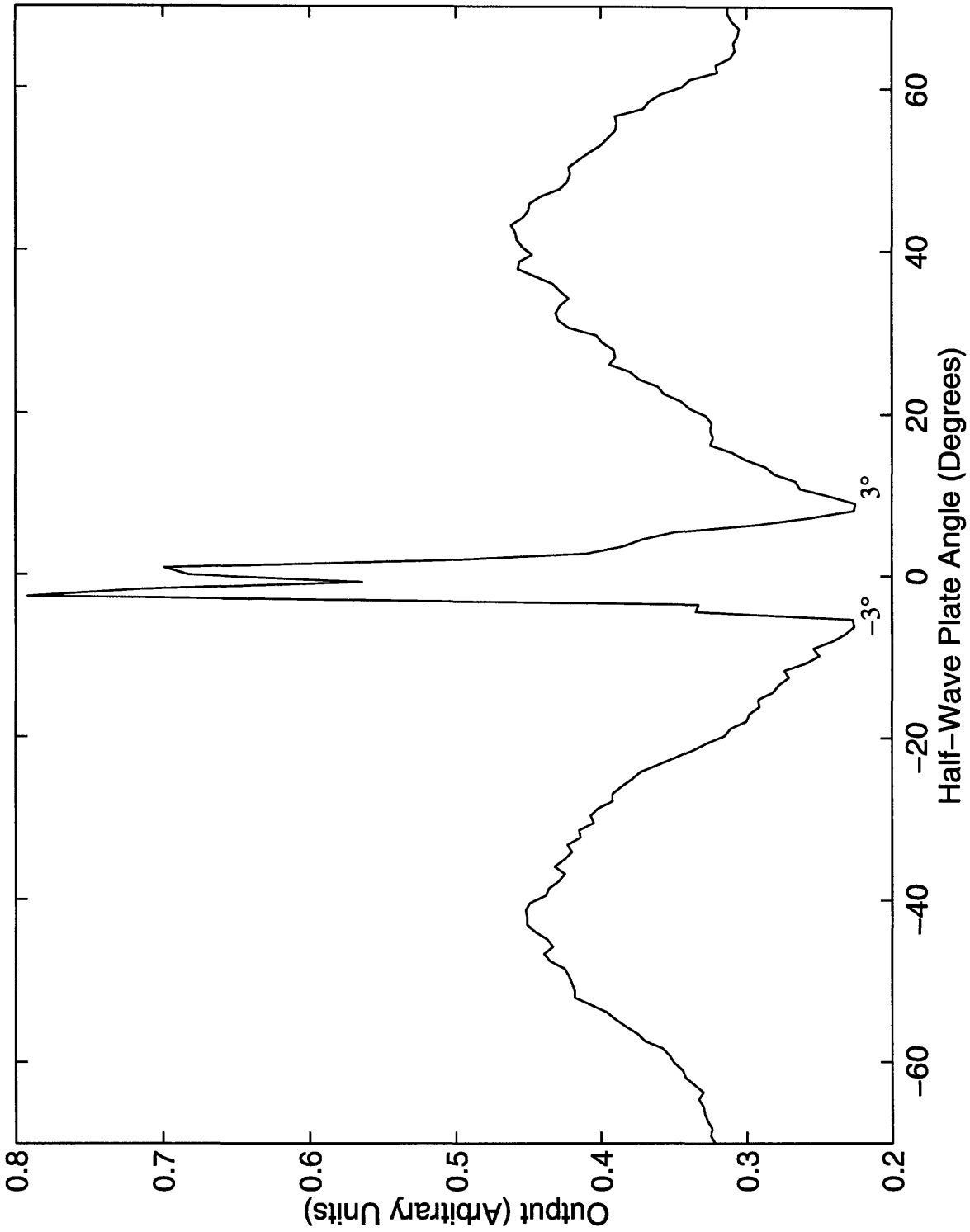


**Figure 5.8:** Dependence of the ring laser cavity output on the polarization of the backward pump.

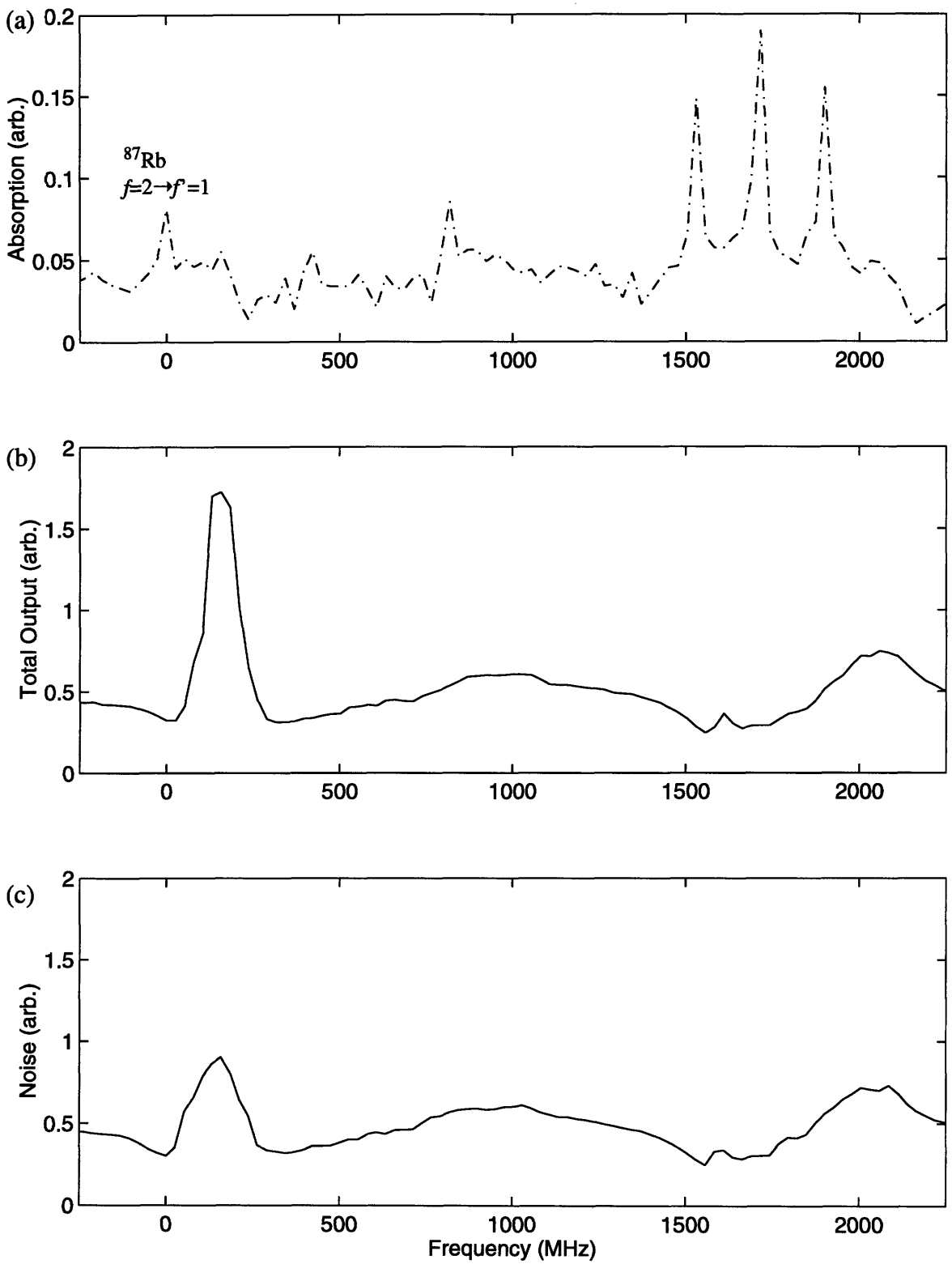


**Figure 5.9:** Dependence of the output of the "standing wave" cavity on frequency. (a) is the saturated absorption signal, (b) is the total output, (c) is the noise output. The units are arbitrary.

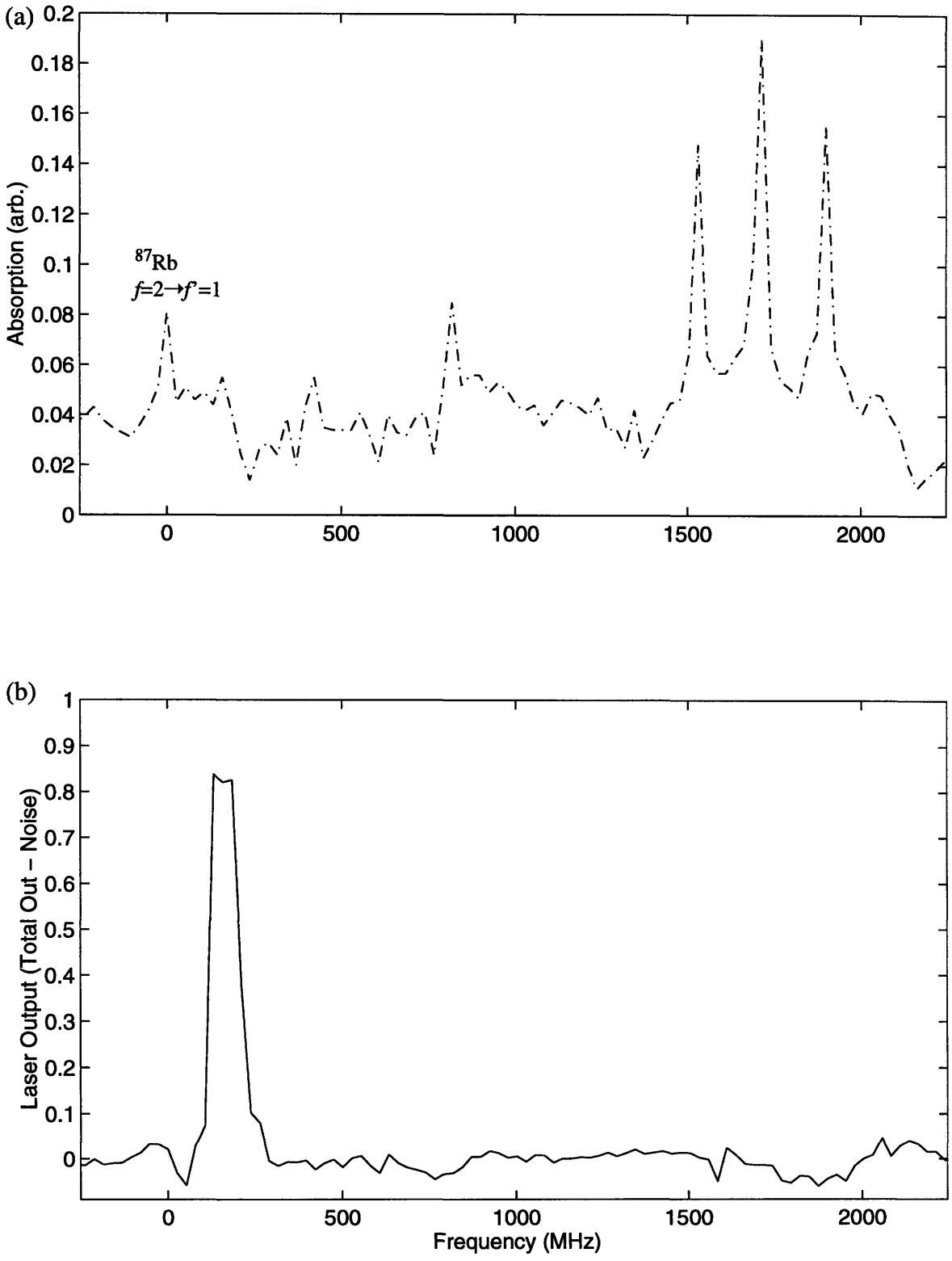


**Figure 5.10:** The difference of the total cavity output and the noise output for the standing wave configuration. (a) is the saturated absorption signal, (b) is the derived output. The units are arbitrary.

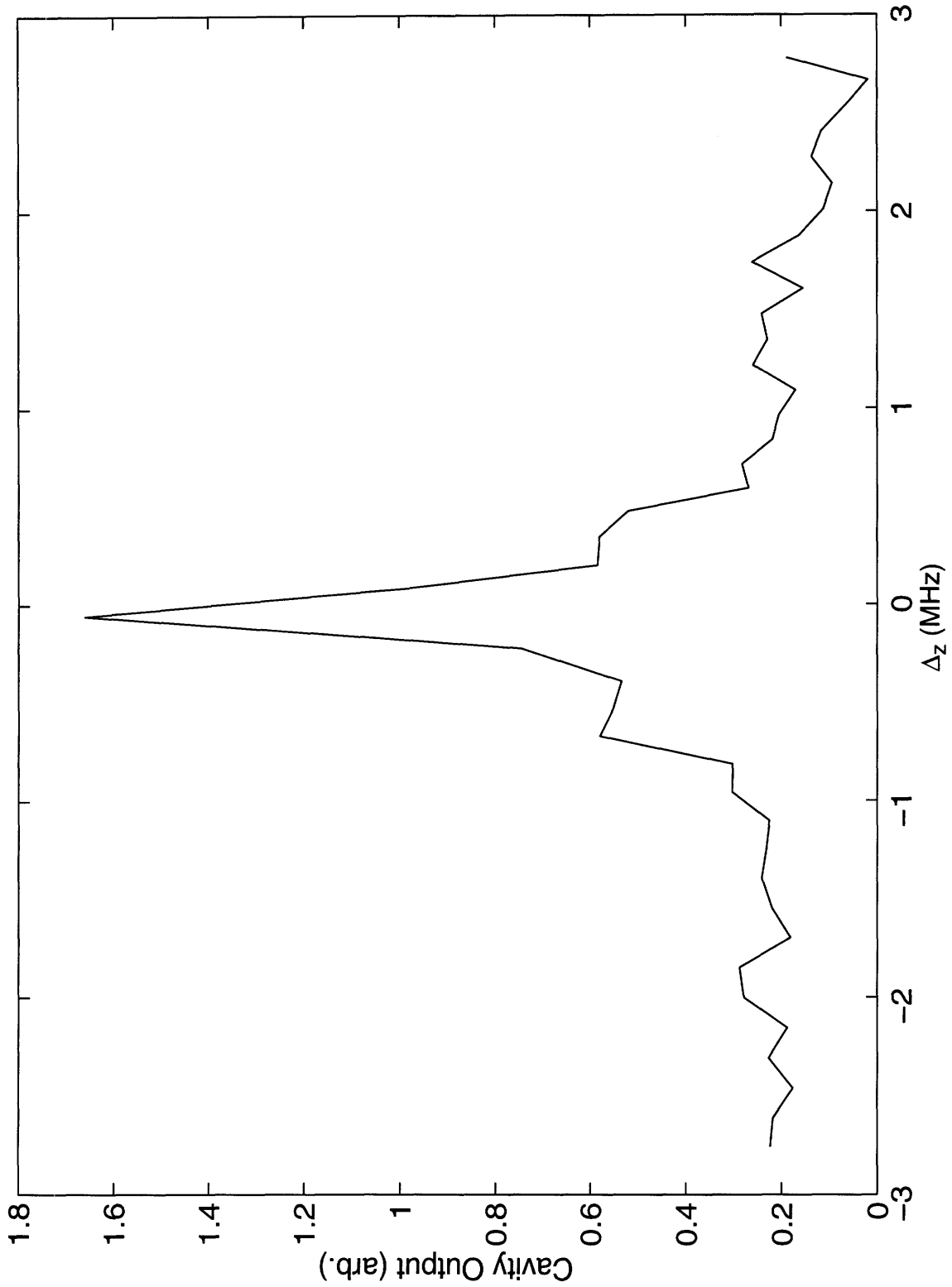


**Figure 5.11:** Dependence of the "standing wave" cavity output on magnetic field.

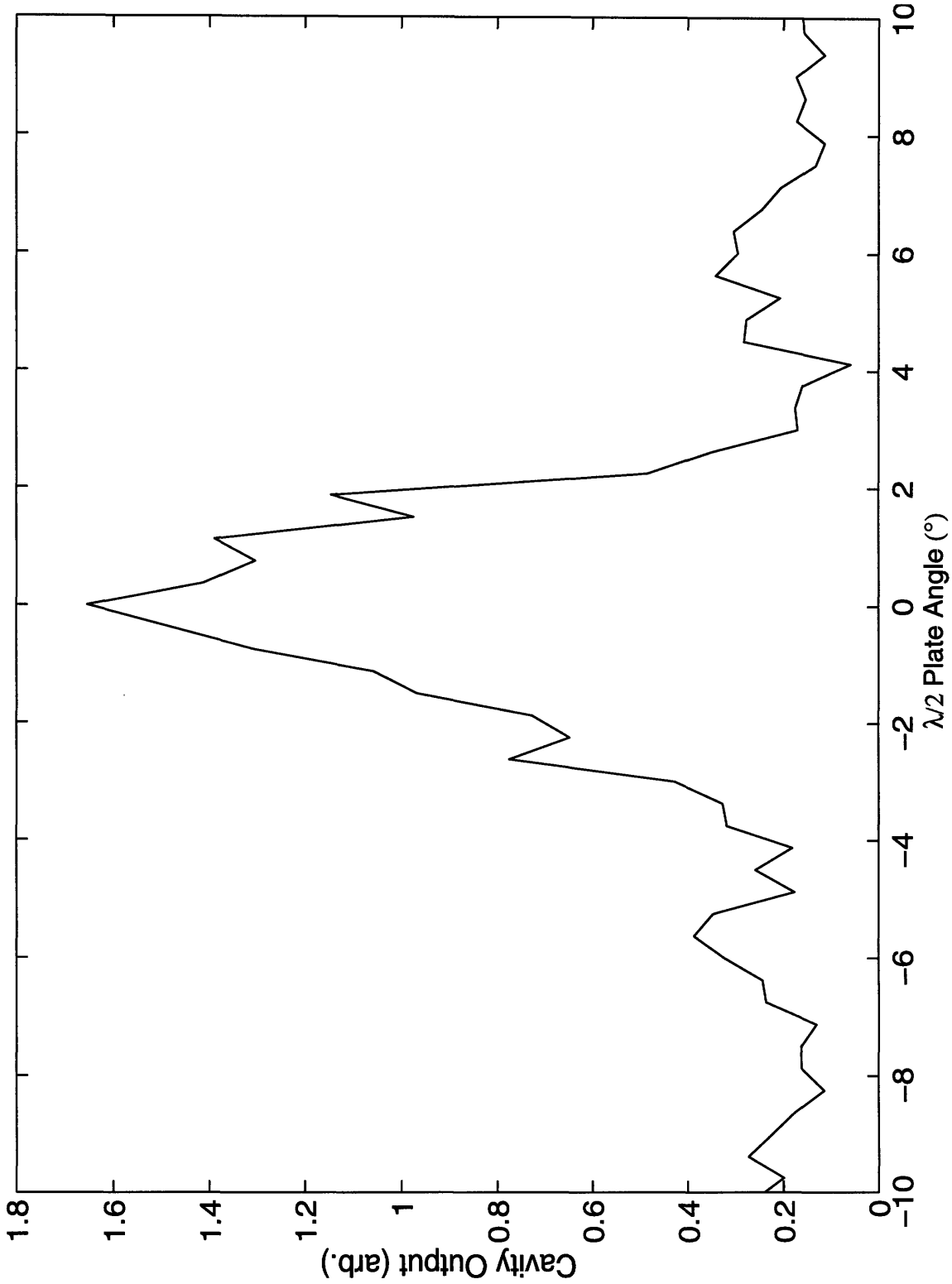


**Figure 5.12:** Dependence of the "standing wave" cavity output on the polarization of the backward pump.

# Chapter 6

# Conclusion

## 6.1 Summary

Optical phase conjugation (OPC) is of interest for many applications. This thesis demonstrates the generation of OPC through degenerate four-wave mixing, which is especially useful for the formation of a phase conjugate laser resonator.

To implement this method, we use a single hyperfine transition between Zeeman sublevels in an atomic vapor of rubidium. Optical pumping with cross-circularly polarized light lets us deal with only a three-level Raman system in the $\Lambda$ configuration. A small detuning from the $D_1$ $5^2S_{1/2}$, $f$=2 $\rightarrow$ $5^2P_{1/2}$, $f$=1 transition in $^{87}$Rb yields the highest efficiency, indicating that nonzero velocity atoms have the highest contribution. Coherent population trapping allows the creation of a coherence grating at lower pump powers in exchange for response time.

Properties of this process make it practical for real applications. This system is fast with a response time of approximately 160 ns. It is also efficient, yielding a gain as high as 40 at low probe power. The system also has low power requirements, requiring far less than 100 mW, making it accessible to semiconductor lasers. The $D_1$ transition in rubidium is also easily attained with semiconductor lasers. This is the first degenerate OPC process to my knowledge which fulfills all of these conditions.

This thesis also documents preliminary work on a phase conjugate ring laser. The use of the PCM in the degenerate case yields an inherent stability in the resonator, a property which is of great interest in the development of laser systems. We obtain lasing at the small detuning from the $5^2S_{1/2}$, $f$=2 $\rightarrow$ $5^2P_{1/2}$, $f$=1 transition.

## 6.2 Future Work

There are many possible directions that can be pursued. The most logical next step is to charaterize and improve the properties of the phase conjugate laser cavity. Specifically, a good starting point is a characterization of the threshold power of the laser. A study of the output power as a function of the overall pump power and as a function of the ratio of the pump powers is also of interest. It is also important to verify the frequency of the resonator cavity.

Achieving a standing wave cavity is of particular interest for the purpose of aberration correction. Further work can either implement the standing wave cavity suggested in this thesis, or attempt to achieve one with exactly counterpropagating pump beams. Since the four-wave mixing scheme can also produce squeezed states of light, an optimization of parameters of the PCM in this thesis may lead to the detection of squeezing.

This scheme can also be attempted in other resonant atomic vapors. Whereas sodium experiments have been done in the past, future work might be attempted in lithium, which has a relevant transition wavelength of 670 nm, or cesium, with a transition at 850 nm. Other non-alkali metals can also be investigated as OPC media.

Finally, on a more practical level, the system can be modified with the intention of bringing it more "down to earth". Semiconductor lasers can be used for the probe and pump beams, and a smaller vacuum system can be made.

# References


[1] Juan F. Lam and Wilbur P. Brown, *Opt. Lett.* **5**, 61 (1980).

[2] T. T. Grove, E. Rousseau, X. Xia, D. S. Hsiung, M. S. Shahriar, P. R. Hemmer, submitted to *Optics Letters*, July 1997.

[3] J. Donoghue, M. Cronin-Golomb, J. S. Kane, P. R. Hemmer, *Opt. Lett.* **16**, 1313 (1991).

[4] M. S. Shahriar, P. R. Hemmer, *Phys. Rev. Lett.* **65**, 1865 (1990).

[5] C. J. Gaeta, J. F. Lam, R. C. Lind, *Opt. Lett.* **14**, 245 (1989).

[6] P. R. Hemmer, D. P. Katz, J. Donoghue, M. Cronin-Golomb, M. S. Shahriar, P. Kumar, *Opt. Lett.* **20**, 982 (1995).

[7] For more information on OPC, a good comprehensive introduction is given in R. A. Fisher, *Optical Phase Conjugation*. New York; Academic Press, 1983.

[8] Boyd, *Nonlinear Optics*. New York; Academic Press, 1992.

[9] A. Yariv, *Optical Electronics, $4^{th}$ edition*. New York; Oxford University Press, 1991.

[10] G. R. Fowles, *Introduction to Modern Optics, $2^{nd}$ edition*. New York; Holt, Rinehart and Winston, 1975.

[11] John Auyeung, D. Fekete, David M. Pepper, Amnon Yariv, *IEEE Journal of Quantum Electronics*, **QE-15**, 1180 (1979).

[12] J. J. Sakurai, *Modern Quantum Mechanics, Rev. edition*. Reading, MA; Addison-Wesley Publishing Company Inc., 1994.

[13] D. Marcuse, *Principles of Quantum Electronics*. New York; Academic Press, 1980.

[14] S. M. Shahriar, P. R. Hemmer, D. P. Katz, A. Lee, M. G. Prentiss, Accepted by *Phys. Rev. A.*, 1996.

[15] E. Rousseau, T. T. Grove, D. S. Hsiung, X. Xia, P. R. Hemmer, M. S. Shahriar, *QELS'97,* OSA Technical Digest Series, Vol 12. Conference Edition, QFC5 (1997).